The Continuum of Wintertime Southern Hemisphere Atmospheric Teleconnection Patterns*,[+]

CHUEH-HSIN CHANG

Research Center for Environmental Changes, Academia Sinica, Taipei, Taiwan

NATHANIEL C. JOHNSON

International Pacific Research Center, SOEST, University of Hawai'i at Mānoa, Honolulu, Hawaii, Scripps Institution of Oceanography, University of California, San Diego, La Jolla, California, and Cooperative Institute for Climate Science, Princeton University, Princeton, New Jersey

ABSTRACT

This study uses the method of self-organizing maps (SOMs) to categorize the June–August atmospheric teleconnections in the 500-hPa geopotential height field of the Southern Hemisphere (SH) extratropics. This approach yields 12 SOM patterns that provide a discretized representation of the continuum of SH teleconnection patterns from 1979 to 2012. These 12 patterns are large in spatial scale, exhibiting a mix of annular mode characteristics and wave trains of zonal wavenumber varying from 2 to 4. All patterns vary with intrinsic time scales of about 5–10 days, but some patterns exhibit quasi-oscillatory behavior over a period of 20–30 days, whereas still others exhibit statistically significant enhanced and suppressed frequencies up to about four weeks in association with the Madden–Julian oscillation. Two patterns are significantly influenced by El Niño–Southern Oscillation (ENSO) on interannual time scales. All 12 patterns have strong influences on surface air temperature and sea ice concentrations, with the sea ice response occurring over a time scale of about 2–4 weeks. The austral winter has featured a positive frequency trend in patterns that project onto the negative phase of the southern annular mode (SAM) and a negative frequency trend in positive SAM-like patterns. Such atmospheric circulation trends over 34 yr may arise through atmospheric internal variability alone, and, unlike other seasons in the SH, it is not necessary to invoke external forcing as a dominant source of circulation trends.

1. Introduction

The Southern Hemisphere (SH) climate has undergone substantial changes over recent decades. A poleward shift of SH westerlies in austral summer (Thompson and Solomon 2002; Marshall 2003; Hande et al. 2012; Young et al. 2011), thought to be strongly related to ozone depletion (Arblaster and Meehl 2006; Polvani et al. 2011; Lee and Feldstein 2013), has manifested itself as an upward trend in positive phase of the southern annular mode (SAM) (Thompson and Wallace 2000; Thompson and Solomon 2002). Both near-surface and midtropospheric air temperature observations and reconstructions show that the Antarctic Peninsula and West Antarctica are among the fastest warming regions globally since the mid-1900s (Steig et al. 2009; Screen and Simmonds 2012; Bromwich et al. 2013). The west Antarctic seas have experienced opposing trends in both sea ice duration and sea ice concentration (SIC), with an increase in the Ross Sea region and decrease over the Bellingshausen Sea and near the Antarctic Peninsula (Stammerjohn et al. 2008; Holland and Kwok 2012; Li et al. 2014). Overall, Antarctic sea ice extent has increased since 1979, in contrast with projections from coupled global climate models (Turner et al. 2013).

In austral winter, similar spatial patterns are seen in both midtropospheric and surface air temperature trends over West Antarctica, likely indicative of the same mechanism responsible for warming in this region (Screen and Simmonds 2012). Analyses of the geopotential height field further reveal an anomalous atmospheric circulation of equivalent barotropic structure over the Bellingshausen–Amundsen Seas and West Antarctica as the southernmost cell of a wave train pattern emanating from the tropics. This poleward arching Rossby wave train can be reproduced by forcing atmospheric general circulation models with tropical sea surface temperature (SST) anomalies (Ding et al. 2011; Li et al. 2014). It is hypothesized that the warm and cold advections induced by the anomalous circulation give rise to warming of the Antarctic Peninsula (Li et al. 2014) and West Antarctica (Ding et al. 2011), as well as the opposing trends in sea ice (Stammerjohn et al. 2008; Li et al. 2014).

The preceding studies illustrate that recently documented changes in Antarctic climate are strongly related to variations in large-scale atmospheric teleconnection patterns. In particular, these patterns tend to be annular in character, as in the SAM, or generally feature poleward arching wave trains, as in the so-called Pacific–South American (PSA) patterns (e.g., Mo and Ghil 1987; Mo and Higgins 1998). Although the intrinsic time scale of these teleconnection patterns is short, on the order of 10 days (Hartmann and Lo 1998; Feldstein 2000b; Gerber et al. 2008; Deser et al. 2010), from the continuum perspective the changes in frequency of occurrence of such patterns can impart substantial interannual and interdecadal climate variations (Franzke and Feldstein 2005; Johnson et al. 2008; Johnson and Feldstein 2010; Lee and Feldstein 2013). As suggested in the discussion above, the frequency of these teleconnection patterns may be influenced by both changes in radiative forcing and slowly varying tropical SST patterns through mechanisms that include stratospheric–tropospheric coupling and the convective excitation of stationary Rossby waves (Hurrell and van Loon 1994; Meehl et al. 1998; Thompson and Solomon 2002; Deser et al. 2010; Ding et al. 2011; Li et al. 2014). However, stochastic variability that is purely internal to the atmosphere in both the tropics (Ding et al. 2014) and extratropics also may impart significant low-frequency variability on interdecadal time scales (Feldstein 2000a).

Although previous studies have described the wintertime variability of the SAM and PSA patterns, such studies generally adopt a discrete modal perspective of these teleconnection patterns. In reality, there likely exists a continuum of SAM-like and PSA-like teleconnection patterns, with each member of the continuum exhibiting variations in spatial structure, temporal evolution, and means of excitation. In this study we use the

method of self-organizing maps (SOMs) (Kohonen 2001; Hewitson and Crane 2002; Johnson et al. 2008) to characterize the austral winter [June–August (JJA)] SH teleconnection patterns. The method of SOMs is a form of cluster analysis that produces a set of representative patterns on a topologically ordered two-dimensional grid. SOMs have been used previously to characterize Northern Hemisphere atmospheric teleconnection patterns (Reusch et al. 2007; Johnson et al. 2008; Johnson and Feldstein 2010) and to characterize SH patterns of zonal wind variability (Lee and Feldstein 2013). This study follows a similar approach as in Johnson et al. (2008), Johnson and Feldstein (2010), and Lee and Feldstein (2013) but for the SH 500-hPa geopotential height field in austral winter. We focus on winter because this season is characterized by strong dynamic variability, and its interdecadal variability has received less attention than the austral summer when ozone depletion is likely to impose stronger forcing on the atmospheric circulation. After determining a set of SOM patterns that describe the continuum of wintertime SH teleconnection patterns, we examine the time scale, composite evolution, links with tropical variability, and connections with temperature and sea ice for each SOM pattern. We then revisit wintertime climate trends since 1979, as in Ding et al. (2011), but from the perspective of changes in the frequency of occurrence of intraseasonal varying teleconnection patterns, as captured by the SOM.

We have organized the paper as follows. Section 2 describes the datasets and methods. In section 3, we present the SOM and the analysis of the intraseasonal, interannual, and interdecadal variability. We provide a summary and conclusions in section 4.

2. Data and methodology

In this section, we first describe the data used in our study, and then we provide a brief overview of the SOM and composites methodology.

a. Data

We use 1979–2012 wintertime (JJA) daily 500-hPa geopotential height anomaly data south of 20°S from the National Centers for Environmental Prediction (NCEP)–National Center for Atmospheric Research (NCAR) reanalysis (Kalnay et al. 1996) for the SOM analysis to characterize the SH teleconnection patterns into a finite number of clusters. In addition, we extract 300- and 700-hPa geopotential height and streamfunction at the 0.2582 vertical sigma level for composite analyses. As described more thoroughly below, we also perform empirical orthogonal function (EOF) analysis

of daily mean zonal mean eddy kinetic energy (EKE), derived from 6-hourly NCEP–NCAR reanalysis zonal and meridional winds from 1000 to 200 hPa and from 20° to 70°S. We calculate anomalies by removing the seasonal cycle, which is defined as the first four harmonics of the calendar day means for the 1981–2010 base period. We weight both the geopotential height and EKE data by the square root of cosine of latitude for the SOM and EOF analyses to account for increasing gridpoint density with latitude. For the EOF analysis of EKE, the data are also weighted by the mass represented by each vertical level.

After generating the SOM patterns, we calculate composite anomaly maps of several variables that are associated with the occurrence of each of the SOM patterns. In particular we calculated composites of NCEP–NCAR reanalysis near-surface air temperature (SAT) and 500-hPa geopotential height [composites derived from the European Center for Medium-Range Weather Forecasts (ECMWF) interim reanalysis (ERA-Interim; Dee et al. 2011) are nearly identical]. We also examine the SOM-related intraseasonal sea ice variability with satellite-derived sea ice concentration (SIC) data from the NASA Goddard Space and Flight Center (GSFC) and the National Snow and Ice Data Center (NSIDC) based on the NASA Team algorithm. This dataset is generated from brightness temperature derived from the Scanning Multichannel Microwave Radiometer (SMMR) on the NASA *Nimbus-7* satellite, the Special Sensor Microwave Imager (SSM/I) on the *F8*, *F11*, and *F13* satellites of the U.S. Defense Meteorological Satellite Program (DMSP), and the Special Sensor Microwave Imager Sounder (SSMIS) on the DMSP *F17* satellite (Cavalieri et al. 1984; Cavalieri et al. 2012). The daily SIC data are interpolated onto a 1° × 1° spatial grid over polar latitudes. This sea ice data source is not associated with known discontinuities that have been identified in the NCEP ice analyses, in the National Oceanic and Atmospheric Administration (NOAA) Optimum Interpolation (OI) SST and the Hadley Centre Ice and Sea Surface Temperature (HadISST) products (Screen 2011), and in the NASA GSFC and NSIDC data based on the bootstrap algorithm (Eisenman et al. 2014). For all datasets used in this study, we calculate anomalies by removing the seasonal cycle in the same way described above.

In the analysis of intraseasonal and interannual variability of the SOM patterns, we investigate the influence of both the Madden–Julian oscillation (MJO) and ENSO on the frequency of occurrence of each of the SOM patterns. For the MJO analysis, we use the Wheeler and Hendon (2004) MJO index, as provided by the Australian Bureau of Meteorology (http://cawcr.

gov.au/staff/mwheeler/maproom/RMM/), which has become a standard index for investigating relationships with the MJO. This index is defined by the two leading principal components (PCs) from an EOF analysis of three combined tropical fields: outgoing longwave radiation (OLR), 850-hPa equatorial zonal wind, and 200-hPa equatorial zonal wind fields. These two PCs, designated as RMM1 and RMM2, define eight MJO phases and an MJO amplitude, which together describe the eastward propagation of the enhanced MJO convection from the African continent (phase 1) to the central equatorial Pacific Ocean (phases 7 and 8), generally over the course of 30–70 days [see Wheeler and Hendon (2004) for plots of the MJO-related OLR fields].

For the ENSO-related analysis, we subdivide all months of the JJA season into one of three standard categories: El Niño, neutral ENSO, or La Niña. We define each category following the conventions of the NOAA/Climate Prediction Center (CPC), which are based on partitioning with the so-called Niño-3.4 SST index. This index is defined by the SST anomaly averaged over the region extending from 5°S to 5°N and from 120° to 170°W, where SST anomalies are derived from the Extended Reconstructed Sea Surface Temperature dataset, version 3b (ERSST; Xue et al. 2003; Smith et al. 2008). Then we classify an El Niño (La Niña) episode when the 3-month running mean Niño 3.4 SST anomaly is greater than 0.5°C (less than −0.5°C) for at least five consecutive overlapping 3-month seasons. All other periods are classified as neutral ENSO.

For the analysis of interdecadal variability, we examine the relationship between the SOM patterns and tropical precipitation. We use pentad precipitation data of the Global Precipitation Climatology Project (GPCP; Adler et al. 2003), which is a precipitation dataset on a 2.5° latitude–longitude grid produced from satellite-derived data and precipitation gauge analyses. We linearly interpolate the pentad data to daily resolution for the composite analyses.

b. SOM analysis

The method of SOMs is a neural network–based cluster analysis, similar to *k*-means clustering that partitions a high-dimensional dataset into a smaller number of representative clusters (Kohonen 2001). In contrast with other types of cluster analysis, these SOM clusters, each of which is associated with a component called a node or neuron, become topologically ordered on a lower-dimensional (typically two-dimensional) lattice so that similar clusters are located close together in the lattice and dissimilar clusters are located farther apart. This topological ordering occurs through the use of a neighborhood function, which acts like a

kernel density smoother among a neighborhood of neurons within this low-dimensional lattice. Consequently, neighboring neurons within this lattice influence each other to produce smoothly varying clusters that describe the distribution of the data used to construct the SOM.

In this study, we perform SOM analysis to categorize daily JJA 500-hPa geopotential height anomalies in the SH poleward of 20°S. In the SOM analysis, the daily geopotential height anomaly field is treated as an M-dimensional vector, where M is the number of grid points. The user specifies the number of clusters K and the method for choosing K is discussed below. The final clustering is determined through an iterative procedure that approximately minimizes the Euclidean distance between the daily geopotential height anomaly fields in M-dimensional space and their best-matching SOM patterns. During this iterative procedure, the SOM patterns also "self-organize" into a topologically ordered two-dimensional lattice or grid, as described above. Each daily height field is assigned to a single best-matching SOM pattern on the basis of minimum Euclidean distance. Lagged composites associated with each geopotential height SOM pattern are calculated on the basis of these assignments of each day to a particular SOM pattern and are discussed in further detail in section 3. Additional details of the SOM methodology can be found in the appendix of Johnson et al. (2008). See also Hewitson and Crane (2002) and Liu et al. (2006) for additional discussion of SOM applications in climate science and typical SOM parameter choices. Reusch et al. (2005) and Liu et al. (2006) compare SOM analysis with empirical orthogonal function analysis for the purpose of pattern extraction, demonstrating several advantages of SOM analysis over the more conventional approach.

As mentioned above, the choice of K must be specified prior to the iterative procedure that determines the SOM clusters. Although there are quite a few approaches for determining an appropriate value of K, there is no universally accepted method for determining the optimal K. Recently, Johnson (2013) proposed a method based on a statistical distinguishability criterion to determine the maximum number of cluster patterns to retain. Under this criterion, the maximum number for K is the maximum value such that all K SOM patterns are statistically distinguishable from each other. This test is administered through the evaluation of whether or not all $K(K-1)/2$ SOM pattern pairs are statistically distinguishable on the basis of a field significance test, which in this case is based on the determination of the "false discovery rate" (Benjamini and Hochberg 1995; Wilks 2006). Additional details of the test are given in Johnson (2013). In the present study, we add two additional steps to ensure

robustness of the results. First, we add a reproducibility criterion: we train the SOM with the first half of the data, then assign the second half to the best matching patterns, and finally evaluate whether the $K(K-1)/2$ SOM composite pairs from the second half of the data are statistically distinguishable. In this way, the SOM training remains separate from the distinguishability test.

The second addition, which also was recently applied in Singh et al. (2014), accounts for the strong autocorrelation evident in daily data. Because a SOM pattern typically persists for several consecutive days, the number of daily occurrences of each SOM pattern would substantially overestimate the number of temporal degrees of freedom in the local t tests that determine whether the SOM pattern composite anomalies are significantly different from each other. To correct for this potential source of bias, we perform the local t tests for subsets of the daily geopotential height fields assigned to each SOM pattern. Because the time scale of atmospheric teleconnection patterns is on the order of one to two weeks (e.g., Feldstein 2000b), we set the condition that each geopotential height field assigned to the SOM pattern within a subset must be separated from all other geopotential height fields within the subset by at least 15 days. If this separation criterion is not met, then we only keep the daily field with the highest pattern amplitude, where the amplitude is defined as the projection of the daily geopotential height field onto the assigned SOM pattern.

The value of K is varied from 2 to 50 at intervals ranging from 2 to 10, and all $K(K-1)/2$ SOM pattern pairs are evaluated for each choice of K. In addition, because the final cluster solutions converge to a local rather than global error minimum, we repeat the calculations five times with different initial cluster seeds for each choice of K. Figure 1 presents the results of the distinguishability test in terms of the number of statistically indistinguishable SOM pattern pairs as a function of K at the 1% significance level. This figure reveals that all SOM pattern pairs remain statistically distinguishable until K reaches a value ~20, at which point some pairs become indistinguishable. This finding suggests that all SOM patterns remain sufficiently distinct for a choice of K less than ~20. Here we choose $K = 12$ because this value is large enough to resolve spatial variations among the continuum of SH teleconnection patterns but small enough that patterns remain statistically distinct and interpretable. The primary results are insensitive to the precise choice of K.

3. Results

In this section we present the results of the SOM analysis, followed by an investigation of the
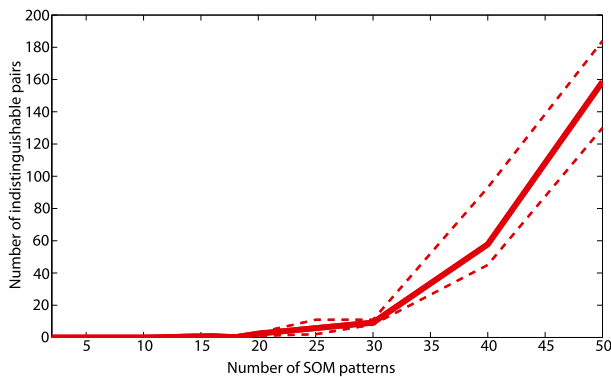
FIG. 1. The number of statistically indistinguishable SOM pattern pairs (*y* axis, 0–200 in increments of 20) as a function of the number of SOM patterns (*x* axis, 0–50 in increments of 5). The bold line is the mean of the five solutions obtained with different random cluster seed initializations, and the dashed lines represent the maximum and minimum from the five solutions. The tests are conducted at the 1% significance level.

intraseasonal, interannual, and interdecadal variations in the SOM pattern frequencies of occurrence. We first present the SOM patterns identified by our analysis that represent the continuum of wintertime (JJA) SH teleconnection patterns in the geopotential height field. Figure 2 shows the 12 unique, statistically distinguishable SOM patterns arranged in a 3 × 4 lattice. The 12 patterns are characterized by large-scale wave train patterns of zonal wavenumbers ranging from 2 to 4. In addition, several patterns clearly project onto the SAM, with plus SAM-like patterns in the bottom-left corner (patterns 5, 6, 9, and 10), and minus SAM-like patterns in the top-right corner (patterns 3, 4, and 8). PSA-like wave train patterns can be seen throughout all SOM patterns, particularly in the top-left and bottom-right corners (patterns 1, 2, 6, 7, 11, and 12). The continuum perspective of Fig. 2 demonstrates that the typical geopotential height patterns in the daily fields cannot be characterized simply by the phase of SAM or the PSA; rather, most SOM patterns represent a mix of these canonical patterns in various phase relationships. The relationship between this SOM analysis and the canonical SH teleconnection patterns is quantified more thoroughly in the following section. The frequencies of occurrence of the 12 SOM patterns are fairly uniform, demonstrating that each pattern occurs with similar frequency (Fig. 2).

Large-scale teleconnection patterns like the SAM and PSA typically are characterized by a deep, equivalent barotropic structure in the extratropics. These 12 SOM patterns generally have a nearly equivalent barotropic structure as well, as evidenced by similar patterns in the composite 300- and 700-hPa anomalies

(Figs. S1 and S2, respectively in supplemental material).

Each of the SOM patterns undergoes substantial variability in frequency across a broad range of time scales. Figure 3 illustrates this point in the form of the time series of 7-yr running mean anomalous frequency of occurrence for each SOM pattern. We derive this time series by calculating the frequency of occurrence of each pattern for each year, subtracting the climatological frequency of occurrence from each annual value, and then smoothing the time series with a 7-yr running mean. We see evidence of strong interannual and decadal variability in the frequencies of occurrence, and a few patterns show a pronounced frequency trend over the past 34 yr. For example, pattern 1 has a tendency for positive anomalous frequency of occurrence in the first half of the record, but negative in the second half. Pattern 4, in contrast, shows the opposite tendency with the highest frequency of occurrence in most recent decade. The following sections describe the intraseasonal, interannual, and interdecadal frequencies of occurrence more thoroughly.

a. Relationship with EOF analysis and the canonical SH teleconnection patterns

As mentioned above, the SOM analysis suggests that the canonical SH teleconnection patterns comprise a mix of annular and wave train–type patterns that occur with similar frequency. These canonical teleconnection patterns typically are identified through EOF analysis of sea level pressure, geopotential height, or upper tropospheric streamfunction, with the first three EOFs defining the SAM (e.g., Thompson and Wallace 2000) and a pair of PSA patterns (e.g., Mo 2000). The two PSA modes depict wavenumber-3 patterns in quadrature with each other and a well-defined wave train from the tropical Pacific to Argentina with large amplitudes in the Pacific–South America sector (Mo and Paegle 2001). We examine the relationship between the 12 SOM patterns and the canonical SH teleconnection patterns by first performing an EOF analysis of the daily JJA 500-hPa geopotential height anomalies and defining the SAM, PSA1, and PSA2 patterns as the first, third, and second EOFs. The first three EOFs explain 10.4%, 7.9%, and 7.1% of the total variance, respectively, and the third is well separated from the fourth by the North et al. (1982) criterion. We notice that the EOF order of the PSA patterns of daily data is the reverse of the previous studies that use low-frequency (e.g., >10 days) data (Ghil and Mo 1991; Lau et al. 1994; Mo and Higgins 1998). This is due to the degenerate nature of the PSA modes (Mo and Higgins 1998; Mo 2000; Robertson and Mechoso 2003). The SAM, PSA1, and PSA2 patterns defined here (Fig. 4) agree well with the patterns
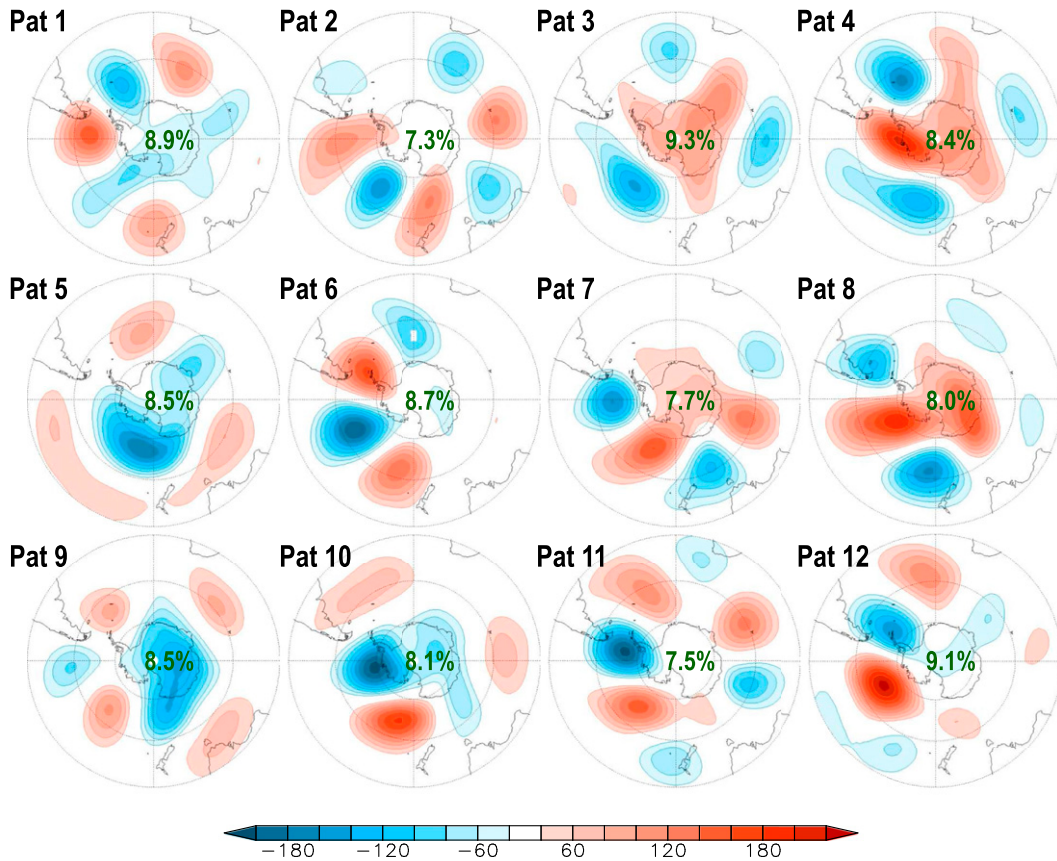
FIG. 2. The 12 SOM patterns of JJA 500-hPa height anomalies arranged in a 3 × 4 array. The colored contours start at ±40 m with an interval of 20 m, and the percentages in the center of each map indicate the frequency of occurrence of the SOM pattern over the 1979–2012 period.

identified in previous studies. One difference is that the SAM defined by the daily data (Fig. 4a) exhibits less zonal symmetry than the SAM typically identified with monthly or seasonal data; however, the daily SAM index (defined below) correlates strongly ($r = 0.90$) with that of the NOAA/CPC (also called the Antarctic Oscillation index and available on their website), which is defined by the projection of daily fields onto the leading EOF of monthly mean 700-hPa height poleward of 20°S. The strong correlation confirms that our definition of the SAM is reasonable.

We next define the daily SAM, PSA1, and PSA2 indices as the standardized PCs of the corresponding EOFs. To determine the relationship between the 12 SOM patterns and these canonical teleconnection patterns, we calculate the composite indices of SAM, PSA1, and PSA2 for each of the 12 SOM patterns by averaging the index values for the days that are assigned to each SOM pattern (section 2b). For the statistical significance calculation of the composite indices, we add the condition that each canonical teleconnection index value must be separated from all others by at least 15 days to

ensure temporal independence. If two occurrences of a particular SOM pattern are separated by less than 15 days, then we discard the teleconnection index values for the day with the lower SOM pattern amplitude,
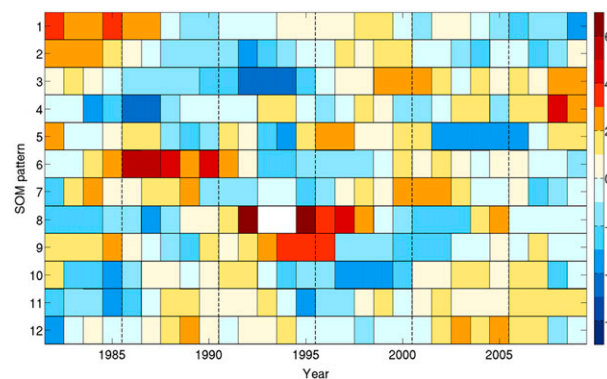

FIG. 3. Seven-year running mean anomalous frequency (color, %) for each of the 12 SOM patterns of Fig. 2. The patterns on the *y* axis run from 1 on top to 12 on the bottom; the years on the *x* axis run from 1995 to 2005; and the color scale runs from +6 (dark red) on top to −6 (dark blue) on the bottom.
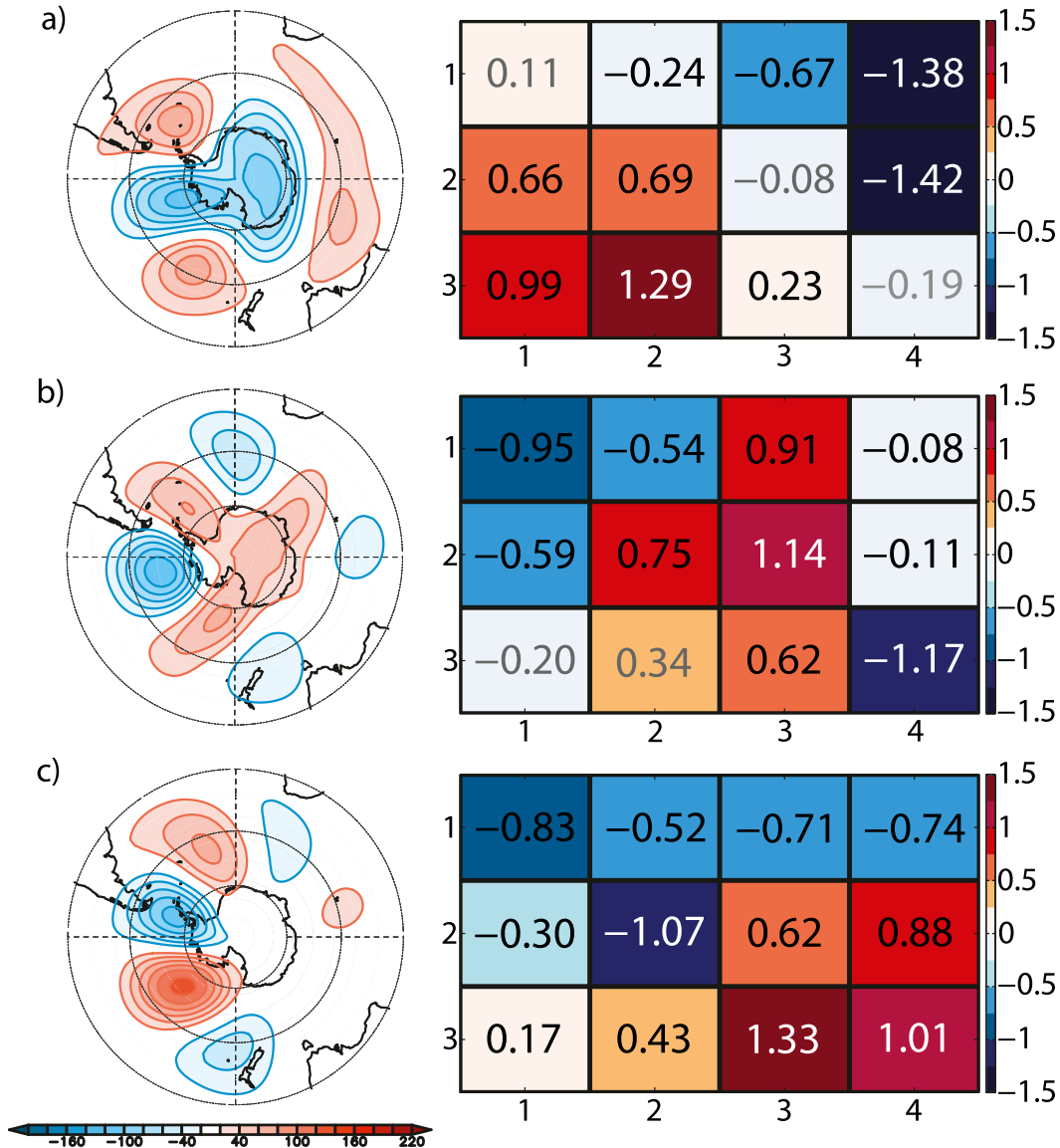
FIG. 4. (left) Canonical SH teleconnection patterns and (right) the composite teleconnection pattern numerical indices (also with color, scale on right) for each of the 12 SOM patterns. The teleconnection patterns shown are the positive phase of the (a) SAM (EOF1), (b) PSA1 (EOF3), and (c) PSA2 (EOF2), and each map represents a regression of 500-hPa geopotential height on the corresponding PC, contoured (color scale on bottom) at intervals of 20 m with the zero contour omitted. The SOM grid on the right side indicates the 12 SOM patterns with the same orientation as in Fig. 2. Black and white composite index numerals are statistically significant at the 5% level, and gray numerals are not statistically significant.

where the pattern amplitude is defined as the projection of the daily 500-hPa height anomaly field onto the SOM pattern. Note that we only discard some index values for the statistical significance calculations but not for the actual reported composite indices. These composite indices of the three teleconnection patterns for all 12 SOM patterns are illustrated in Fig. 4.

The results in Fig. 4a confirm that patterns in the left (right) half of the SOM generally are associated with the

positive (negative) phase of the SAM. In particular, four patterns in the bottom left (patterns 5, 6, 9, and 10) are most strongly associated with the positive SAM, and three patterns in the top right (patterns 3, 4, and 8) are most strongly associated with the negative SAM. Figure 4b demonstrates that the middle of the SOM (patterns 3, 6, 7, and 11) projects most strongly onto the positive phase of the PSA1, whereas both the top left (patterns 1, 2, and 5) and bottom right (pattern 12)

project onto the negative phase. PSA2 is partitioned most strongly along the bottom left to top right diagonal (Fig. 4c), with patterns in the bottom right (patterns 8, 11, and 12) associated with the positive phase and patterns in the top left (patterns 1 and 6) most strongly related with the negative phase.

The preceding analysis suggests that each of the three canonical SH teleconnection patterns, as determined through EOF analysis, can be described as a mix of three to five SOM patterns that occur with similar frequency. To support this assertion quantitatively, we compare each of the three EOF patterns with its corresponding mixed SOM patterns, where the mixed SOM patterns are defined as a frequency-weighted sum of a subset of SOM patterns. The subset consists of all SOM patterns whose composite teleconnection index (i.e., the values shown in Fig. 4) is greater (less) than 0.5 (-0.5) for the positive (negative) phase of the corresponding EOFs. Specifically, we calculate

$$z_T(x, y) = c \sum_{i=1}^{N} f_i z_i(x, y), \qquad (1)$$

where z_T is the mixed SOM patterns of 500-hPa height for teleconnection pattern T (SAM, PSA1, or PSA2) of either positive or negative phase, z_i is SOM pattern i within the subset defined above, f_i is the frequency of occurrence of SOM pattern i, and N is the total number of SOM patterns within the subset, ranging from 3 to 5. The factor c is defined as

$$c = \left(\overline{PC_T} \sum_{i=1}^{N} f_i \right)^{-1}, \qquad (2)$$

where $\overline{PC_T}$ is the mean PC index amplitude for teleconnection pattern T within the subset. This factor is a normalization to facilitate direct comparison between the EOF regression patterns and the corresponding mixed SOM patterns, determined by Eq. (1). Both are interpreted as anomalies with respect to an index amplitude of one standard deviation.

As seen in Fig. 5, the PC regressions and their corresponding mixed SOM patterns, z_T, display striking similarities. The strong correspondence between the PC regressions, representing the canonical teleconnection patterns (left), and z_i, the mixed SOM patterns (center and right), indicates that both the positive and negative phases of the SAM, PSA1, and PSA2 can be captured by a linear combination of three to five SOM patterns. The SOM patterns, however, have the advantage of bearing a stronger resemblance to the daily 500-hPa geopotential height anomaly patterns that comprise the subset. To illustrate this point, we calculate the mean

centered pattern correlation (e.g., Santer et al. 1993) between the daily 500-hPa height anomaly fields with a standardized PC amplitude exceeding 0.5 and the corresponding EOF pattern. The mean absolute pattern correlations for the SAM (EOF1), PSA1 (EOF3), and PSA2 (EOF2) are 0.36, 0.30, and 0.31, respectively. We also performed similar pattern correlation calculations for the daily 500-hPa height anomaly fields that comprise the 12 SOM clusters. The mean pattern correlation for the 12 SOM patterns is 0.46, with values ranging from 0.42 to 0.50. This calculation demonstrates a greater correspondence between the daily anomaly fields and each of the SOM patterns than that between the daily fields and any of the first three EOFs.

b. Intraseasonal variability

On the basis of previous teleconnection pattern studies (e.g., Feldstein 2000b), we expect that each of the 12 SOM patterns of Fig. 2 would have an intrinsic time scale on the order of one to two weeks. To investigate this hypothesis thoroughly and to document the typical evolution of each pattern and its influence on temperature and sea ice, we calculate lagged composites based on an amplitude time series assigned to each SOM pattern. The amplitude time series is calculated by projecting all daily JJA 500-hPa height (Z500) anomaly patterns onto the patterns shown in Fig. 2, and then standardizing the resulting time series. We then calculate lagged composites of the amplitude time series as well as spatial fields of Z500, SAT, and sea ice concentration anomalies for each SOM pattern. The zero lag is defined by the occurrence of the particular SOM pattern, and if the pattern occurs for several consecutive days, then the day with the largest amplitude within the sequence is assigned a lag of zero. To generate reasonable confidence that episodes are independent for the composite, we add the condition that all identified episodes for a particular SOM pattern must be separated by at least 15 days using the method described in the previous section. Statistical significance of the composite amplitude time series is calculated on the basis of a two-sided t test at the 5% significance level.

Here we present the lagged composite maps for three patterns that represent typical life cycle behavior. The lagged composites for the rest of the patterns can be found in the supplementary material (Figs. S3–S11). Figures 6–8 show the evolution of anomalous Z500, SAT, and SIC for patterns 1, 6, and 8 from lag -6 days to lag $+6$ days with an interval of 3 days. We focus on SAT and SIC in connection with these SOM patterns owing to the close relationships among these variables. To isolate the intraseasonal SIC variability from lower-frequency SIC variability, we show
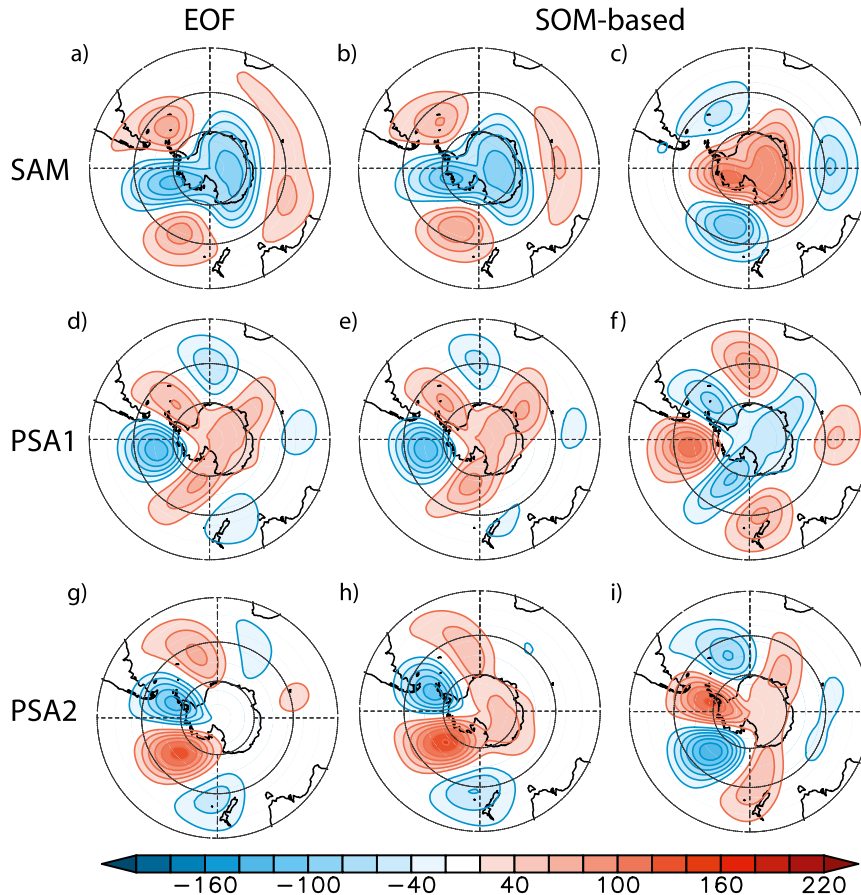
FIG. 5. Canonical SH teleconnection patterns determined (left) through EOF analysis and (center),(right) as a linear combination of SOM patterns determined with Eq. (1). Shown are the PC regressions (colors, m) for the (a) SAM (EOF1), (d) PSA1 (EOF3), and (g) PSA2 (EOF2), with the same plotting conventions as in Fig. 4, together with the (b),(e),(h) positive phase and (c),(f),(i) negative phase SOM-based reconstructions of the SAM, PSA1, and PSA2, respectively.

composites of ΔSIC, which is defined as change of the sea ice concentration anomaly composite with respect to the composite value at the time of each pattern onset, defined below.

Inspection of Figs. 6a, 7a, and 8a confirms that the SOM patterns grow and decay over a period of about one week. Here we define the time scale of each SOM pattern as the time between onset and decay, where onset is defined as the time when the pattern amplitude first reaches $1/e$ times the peak amplitude, and decay is the time when the amplitude falls to $1/e$ times the peak amplitude. Table 1 shows that the time scale of the SOM patterns ranges from 4.9 to 8.5 days.

All three composite life cycles in Figs. 6–8 indicate that a wave train pattern is initiated at about a lag of −6 days (Figs. 6b, 7b, and 8b). The wave train patterns intensify until lag 0 and propagate slowly eastward until lag 3. Following the evolution of the wave train, SAT

anomalies of alternating signs develop in approximate spatial quadrature with the atmospheric highs and lows (Figs. 4–6), consistent with the expected pattern of cold and warm advection associated with the atmospheric circulation. ΔSIC becomes prominent around lag −3 days, with +ΔSIC coincident with the cold SAT anomaly and northward wind forcing, and vice versa (Figs. 6c, 7c, and 8c). The amplitude of ΔSIC reaches maximum between lag 0 and lag +3 (Figs. 6d, 7d, and 8d).

The lagged composites in Figs. 6–8 indicate that the SIC anomalies undergo substantial growth and decay on intraseasonal time scales in response to the forcing of large-scale atmospheric teleconnection patterns. The role of atmospheric circulation revealed in the composite maps is consistent with the wind-driven dynamic and thermodynamic arguments of several studies (Stammerjohn et al. 2008; Ding et al. 2011; Bromwich
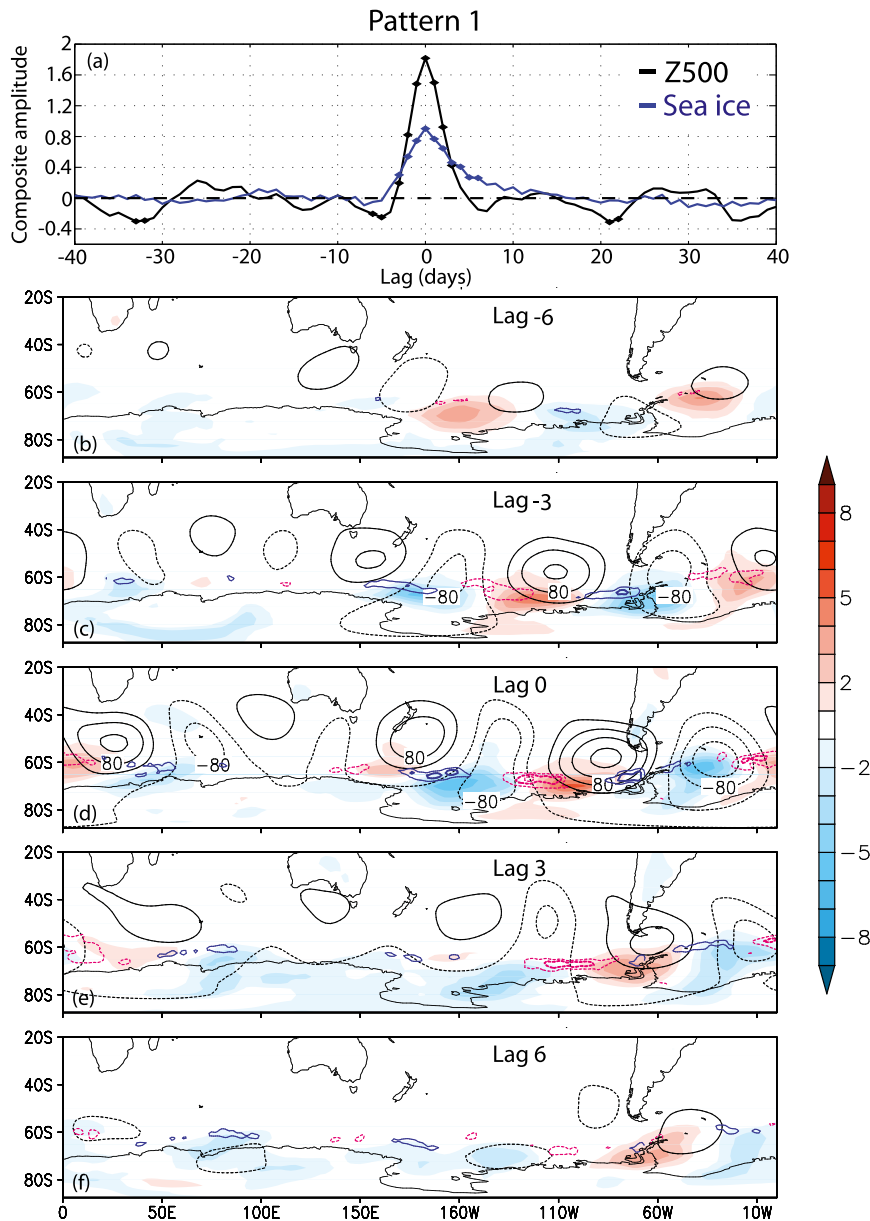
FIG. 6. (a) Lagged composites of the SOM 500-hPa height (black) and SIC (blue) amplitude time series, as defined in the text, for SOM pattern 1 and lags between −40 and +40 days. The symbols on the curves represent statistically significant amplitudes at the 5% level on the basis of a two-sided t test. (b)–(f) Composites of 500-hPa height anomalies (black contours at an interval of 40 m), SAT anomalies (color shading, °C), and ΔSIC (red and blue contours at an interval of 3%) for lags of (b) −6, (c) −3, (d) 0, (e) +3, and (f) +6 days. Dashed contour lines indicate negative values, and blue (red) contours indicate positive (negative) ΔSIC. Note that the thick blue (red) contours denote ΔSIC = 6% (−6%).

et al. 2013; Holland and Kwok 2012; Li et al. 2014). In the same way that we define an amplitude time series for the SOM 500-hPa height pattern, we define a SOM-related SIC amplitude time series by projecting the daily SIC anomaly fields onto the lag-0 composite SIC anomaly map for each SOM pattern. The composite SIC

amplitude time series is shown in blue in Figs. 6a, 7a, and 8a. These time series indicate that the SIC response also grows and decays on short, intraseasonal time scales but over a longer time scale than that of the midtropospheric circulation. Table 1 shows that the SIC pattern time scales, defined in the same way as for the 500-hPa height
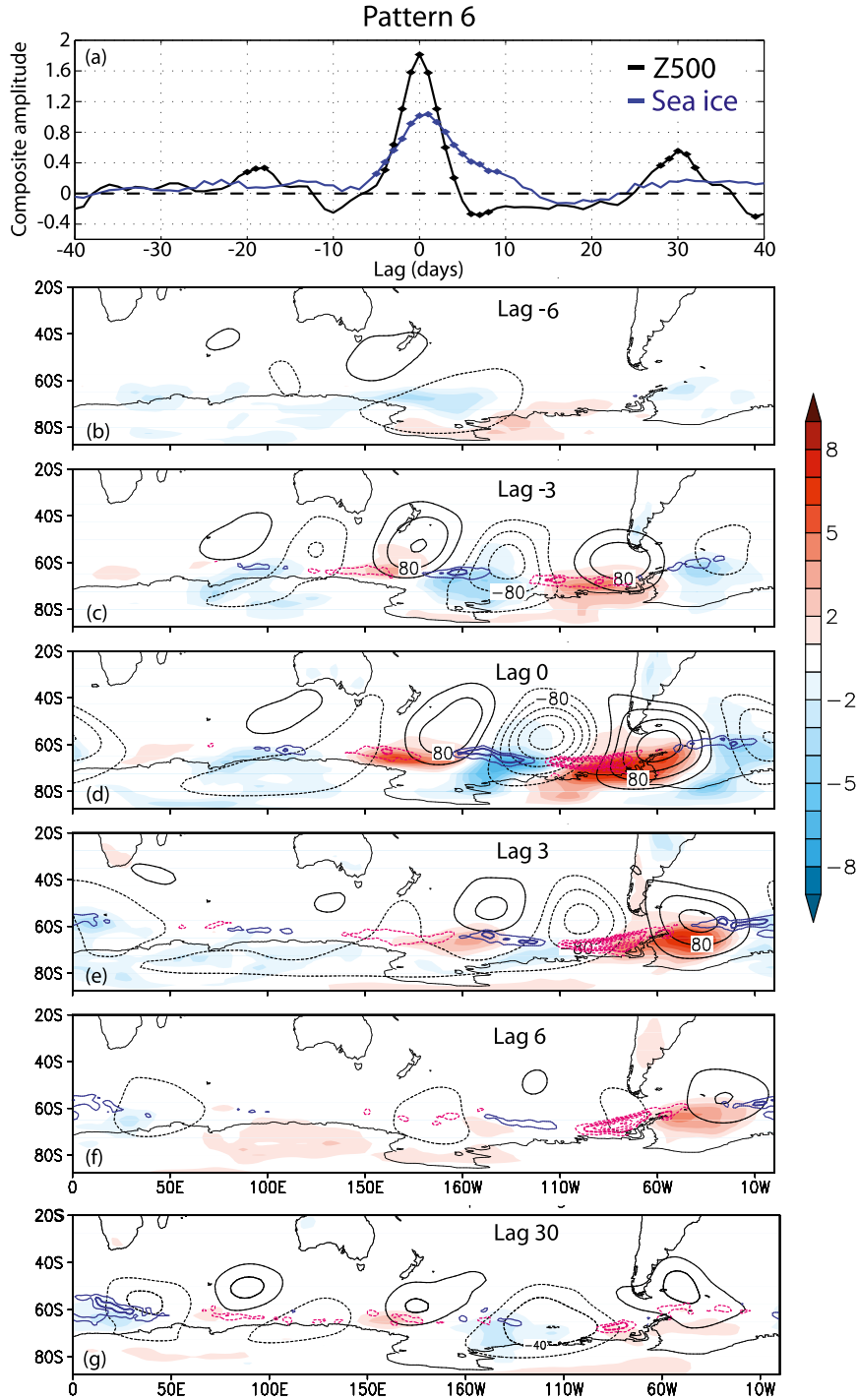
Pattern 6

FIG. 7. (a)–(f) As in Fig. 6, but for SOM pattern 6. (g) As in (a)–(f) but for a lag of +30 days with 500-hPa height anomalies in black contours at an interval of 20 m and ΔSIC in red and blue contours at an interval of 2%. The thick blue (red) contours denote ΔSIC = 4% (−4%).

time scales, are about 2–4 times longer than the 500-hPa height time scales. The longer time scale of SIC pattern growth and decay likely relates to the slower processes regulating anomalous radiative and surface heat fluxes that act in tandem with the faster mechanical forcing associated with the growth and decay of the Z500 pattern. For example, in a study of the MJO impact on Arctic SAT, Yoo et al. (2012b) demonstrate that the
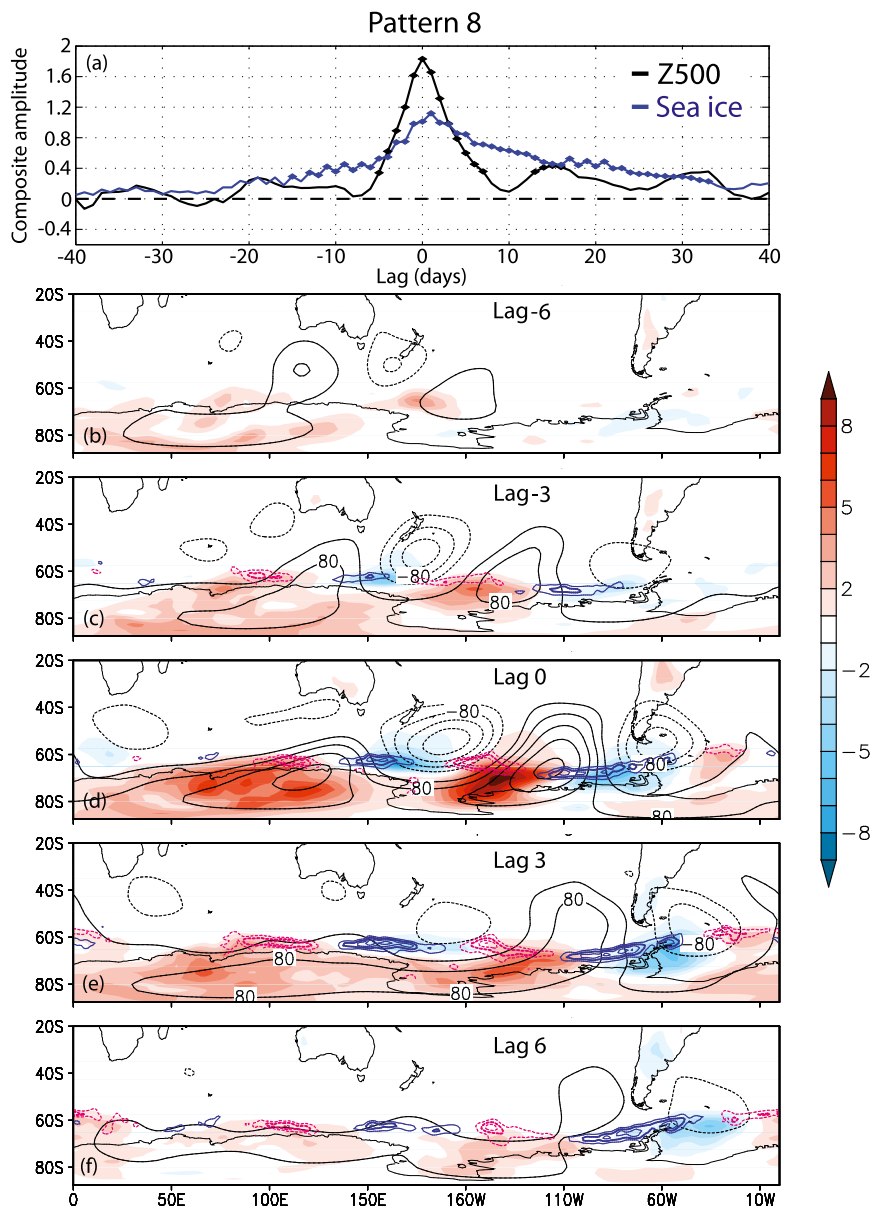
FIG. 8. As in Fig. 6, but for SOM pattern 8.

poleward flux of moisture and resulting increase in downward infrared radiative flux act to prolong MJO-related Arctic SAT change after the large-scale atmospheric circulation anomaly pattern decays. These results agree with earlier findings of Lee et al. (2011). A more detailed understanding of the mechanisms regulating the time scale of SIC anomaly pattern evolution requires further study.

Although Figs. 6–8 share many common features, there are some notable differences among SOM patterns as well. In particular, pattern 6 exhibits some surprising evidence of oscillatory behavior over a time scale

of ∼(20–30) days (Fig. 7a). The composite amplitude time series exhibits statistically significant peaks at a lag of ∼−20 and ∼+30 days. Figure 7g illustrates the lag +30-day composites, which resemble the atmospheric wave train evident at lag 0 but of weaker amplitude. As described below, we examine the possible role of the MJO in modulating the frequencies of occurrence of the SOM patterns, but pattern 6 does not exhibit a strong relationship with the MJO (not shown). Recently, however, Thompson and Woodworth (2014) and Thompson and Barnes (2014) provided strong evidence that the Southern Hemisphere atmospheric

TABLE 1. Time scale of each of the SOM patterns and the associated sea ice composite patterns, as defined in the text.

SOM pattern No.	SOM pattern time scale (days)	SIC time scale (days)
1	6.3	11.0
2	4.9	8.8
3	5.9	16.8
4	6.1	13.5
5	7.1	19.6
6	5.3	15.7
7	5.8	21.7
8	4.8	7.5
9	8.5	35.7
10	7.6	15.7
11	5.1	14.1
12	7.3	12.3

circulation exhibits periodic behavior with a time scale of 20–30 days in association with the so-called baroclinic annular mode (BAM). This distinct periodicity, which is evident in both observations and a hierarchy of models (Thompson and Barnes 2014), is believed to result from feedbacks between eddy heat fluxes and baroclinicity and manifests as pulses of extratropical eddy kinetic energy.

The lagged composites of Fig. 7 suggest that the occurrence of SOM pattern 6 is associated with a pulse of baroclinic eddy growth. Therefore, we speculate that the periodicity evident in Fig. 7a may be a signature of the BAM. Similar periodicity, though weaker but still significant, is also evident in SOM pattern 2 (Fig. S3). To explore the possible link with the BAM, we first calculate the BAM index in the same way as in Thompson and Woodworth (2014) except that we restrict focus to JJA instead of the whole year. Specifically, we define the BAM index as the leading, standardized PC of daily zonal-mean EKE, $[u^{*2} + v^{*2}]/2$, from 1000 to 200 hPa, where the square brackets indicate the zonal mean and asterisks denote departures from the zonal mean. Figure 9a shows the regression of zonal-mean EKE on the BAM index, which agrees well with the pattern in Thompson and Woodworth (2014; their Fig. 2f) except for the equatorward shift of the upper tropospheric maximum; this difference likely relates to the stronger subtropical jet in JJA relative to the annual mean. We next calculate lagged composites of the BAM index using the same approach as for the composite projection indices in Figs. 6a, 7a, and 8a. In Fig. 9b, we illustrate the lagged composite BAM index for patterns 6 and 12, as pattern 12 resembles the opposite phase of pattern 6 (see Fig. 2). Consistent with our speculation, we see positive composite BAM index values at lag 0, indicating enhanced zonal-mean EKE, and quasi-oscillatory behavior with statistically significant peaks at lags of

20–30 days. We note that the secondary peak in the composite projection index for pattern 6 ($\sim$+30 days; Fig. 7a) is later than the peak in the BAM index ($\sim$+25 days; Fig. 9b). This offset may reflect the limitation of using a single PC to capture the dynamical processes of the BAM, but the quasi-oscillatory behavior in both time series is intriguing.

We also note that pattern 12 does not show a similar peak in the projection index for lags of 20–30 days (Fig. S11a) despite the peak in the BAM index. Inspection of the lag +25-day composite 500-hPa height anomalies for pattern 12 (not shown) reveals an invigorated wave train in the southern Indian Ocean and western Pacific, similar in pattern but opposite in phase to the lag +30-day composite for pattern 6 (Fig. 7g) but amplitudes are weak over the main South Pacific and South Atlantic action centers. This example highlights that quasi-oscillatory spatial variability of the SH circulation in association with the BAM may be more complicated than recurrence of a single pattern. Moreover, these patterns associated with the BAM revealed here do not resemble annular modes; instead they feature zonally extended wave trains. Therefore, the annularity evident in the composite zonal wind field associated with the BAM (Thompson and Woodworth 2014; see their Fig. 10b) likely is a weak residual pattern not closely resembling the individual BAM episodes. These observations suggest that the quasi-oscillatory variability of the SH circulation in association with the BAM requires further study for us to understand the spatial patterns in association with pulses of zonal EKE anomalies.

Another potential source of predictability at similar lead times is the MJO, which is the dominant mode of tropical variability on intraseasonal time scales that is characterized by large-scale convection anomalies that circumnavigate the tropical belt in approximately 30–70 days (Madden and Julian 1971, 1972; Zhang 2005). The MJO extratropical influence occurs primarily through the tropical excitation of poleward-propagating Rossby waves (e.g., Hoskins and Karoly 1981), and the MJO has well-known impacts on large-scale wintertime teleconnections in the Northern Hemisphere (e.g., Ferranti et al. 1990; Cassou 2008; Mori and Watanabe 2008; L'Heureux and Higgins 2008; Lin et al. 2009; Johnson and Feldstein 2010; Riddle et al. 2013) as well as in the Southern Hemisphere (Revell et al. 2001; Matthews and Meredith 2004; Yoo et al. 2012a).

In this study, we examine the MJO influence on the SOM pattern frequency of occurrence in a similar way as in Cassou (2008) and Riddle et al. (2013) for Northern Hemisphere teleconnection patterns identified through cluster analysis. We first identify all active MJO periods
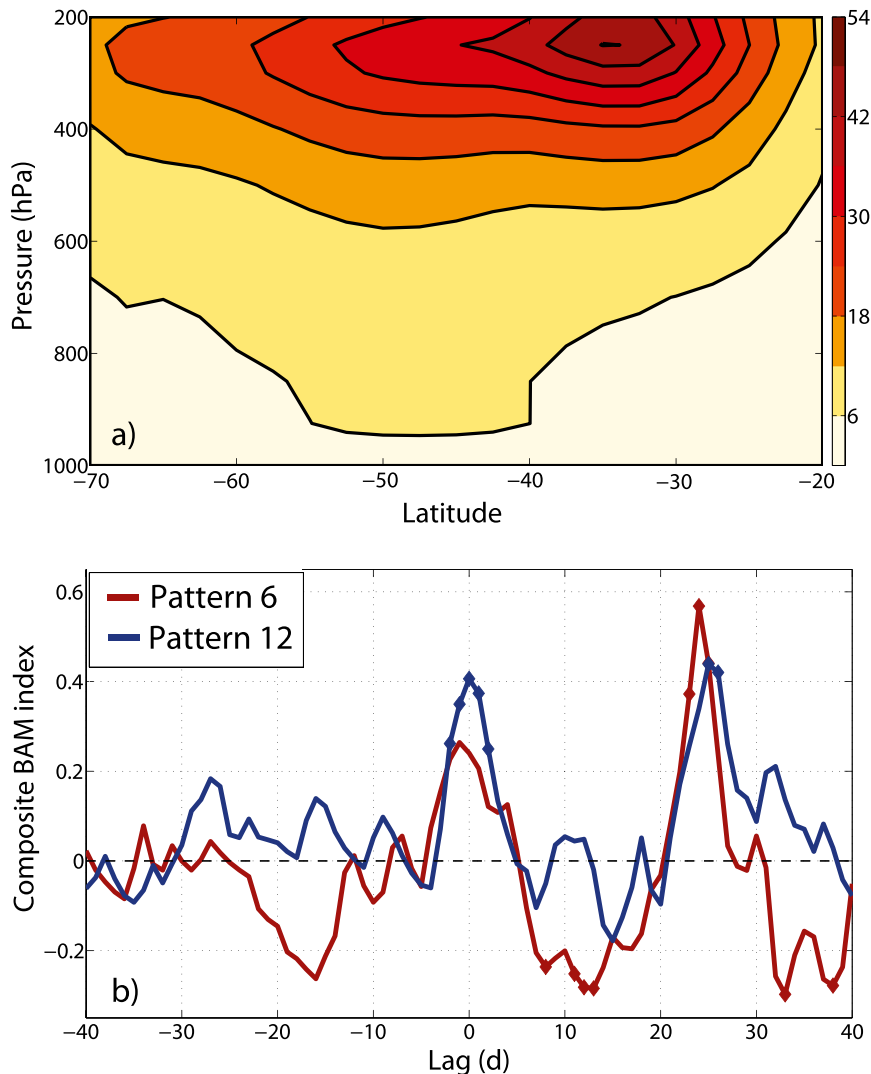
FIG. 9. (a) Regression of JJA zonal mean eddy kinetic energy ($m^2\,s^{-2}$) on the BAM index, which is defined as the leading standardized PC of JJA SH eddy kinetic energy. (b) Lagged composite amplitude of the BAM index for SOM patterns 6 (red) and 12 (blue) for lags between -40 and $+40$ days. The symbols on the plots indicate statistically significant composite amplitudes at the 5% level based on a two-sided t test.

corresponding with each of the eight Wheeler and Hendon (2004) MJO phases, where an active MJO is defined by an amplitude exceeding 1.0. We recognize that this amplitude criterion does not necessarily isolate all "true" MJO episodes with eastward propagating convection at the characteristic MJO time scale, but the more inclusive definition used here likely would be beneficial from a forecasting perspective (e.g., Johnson et al. 2014). Then we calculate the anomalous frequency of occurrence of each SOM pattern for lags ranging from two days before (lag -2 days) to 42 days after the MJO phase occurrence (lag $+42$ days). We next smooth the anomalous frequency time series with a 5-day running

mean. Here we express anomalous frequencies as an anomalous percentage relative to climatology, as in Cassou (2008) and Riddle et al. (2013), so that a value of -100% means no pattern occurrence and a value of $+100\%$ means twice as frequent occurrence as in climatology.

We evaluate the statistical significance of the anomalous frequencies through a Monte Carlo simulation approach. For each simulation, we randomly shuffle the years of both the SOM pattern occurrence and MJO time series and then calculate the anomalous frequencies of occurrence in the same way as with the true SOM pattern occurrence and MJO time series. We repeat
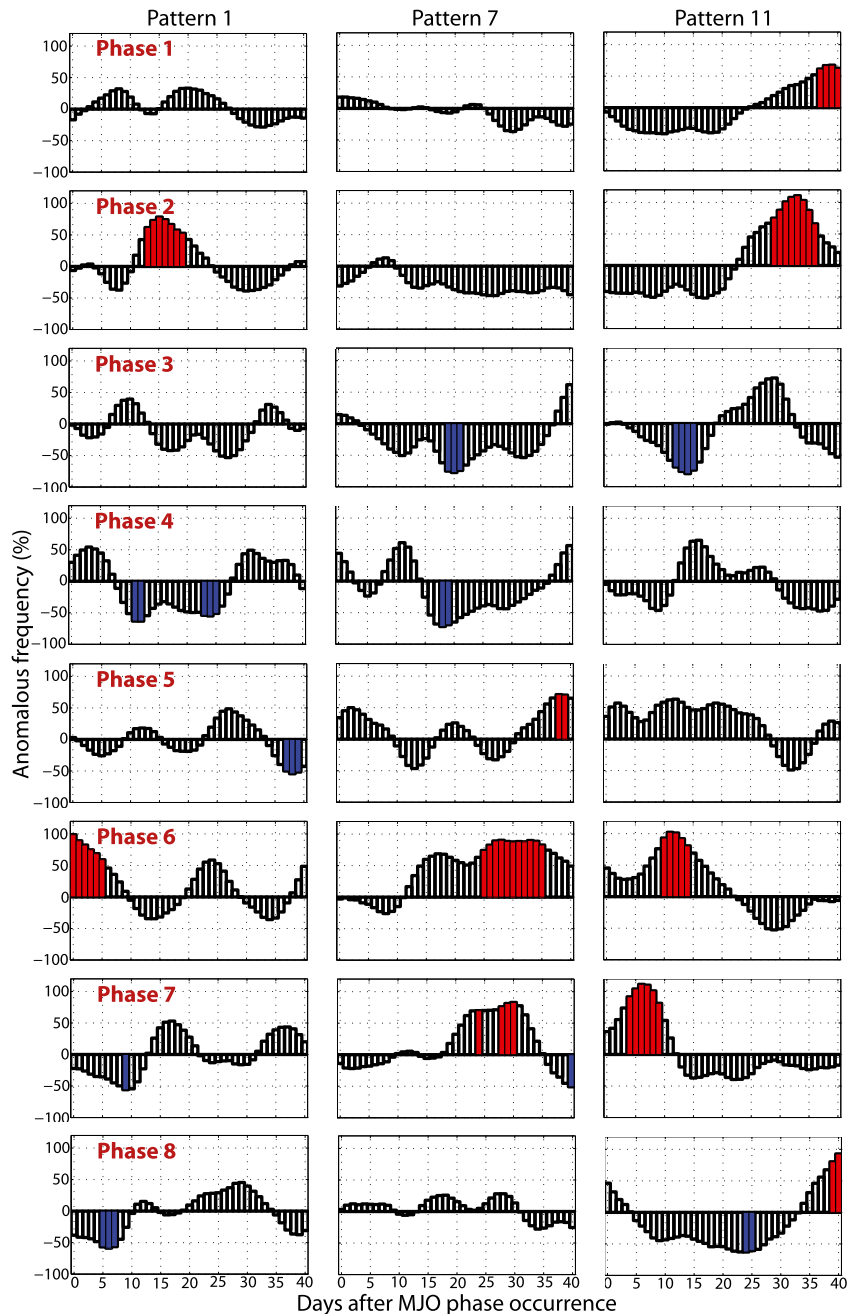
FIG. 10. Anomalous frequencies of occurrence (*y* axes, %) of SOM patterns (left) 1, (center) 7, and (right) 11 as a function of (top)–(bottom) MJO phase and lag (*x* axes, days). Red (blue) filled bars represent anomalous positive (negative) anomalous frequencies at the 5% significance level.

these simulations 10 000 times and calculate the 2.5th and 97.5th percentiles of the synthetic anomalous frequencies for each lag, MJO phase, and SOM pattern. The SOM pattern anomalous frequencies are considered statistically significant at the 5% level if they are below the 2.5th or above the 97.5th percentiles of the distribution of simulated frequencies.

After performing these calculations, we identify three SOM patterns for which the MJO has a notable influence: patterns 1, 7, and 11. Figure 10 presents the anomalous frequencies of these three patterns as a function of MJO phase and lag. This figure suggests that pattern 1 is strongly excited about 15–20 days after the MJO is in phase 2 (Fig. 10, left column), when positive anomalous

convection occurs over the tropical Indian Ocean and suppressed convection occurs over the western equatorial Pacific (Wheeler and Hendon 2004; see also the NOAA/CPC tropical MJO composites page at their website www.cpc.ncep.noaa.gov). In contrast, pattern 1 occurrence tends to be suppressed about 10–25 days after the MJO is in phase 4, when the anomalously strong convection progresses to the western equatorial Pacific region.

Pattern 7 similarly experiences suppressed occurrence in association MJO phases 3 and 4 (Fig. 10, center panels), but the strongest excitement appears to occur about 25–35 days after the MJO is in phase 6, when there is an east–west dipole with suppressed convection in the tropical Indian Ocean and enhanced convection throughout the equatorial Pacific region. Pattern 1 projects onto the positive phase of the SAM, whereas pattern 7 projects onto the negative phase. The results presented here suggest that an east–west dipole of tropical convection with enhanced convection in the Indian Ocean and suppressed convection over the western equatorial Pacific excites a positive SAM-like pattern, whereas the opposite phase of the convection dipole excites a negative SAM-like pattern. This general relationship is consistent with previous studies (Matthews and Meredith 2004; Flatau and Kim 2013; Zhang 2013), and a similar relationship exists in the Northern Hemisphere with the northern annular mode (L'Heureux and Higgins 2008; Riddle et al. 2013).

The MJO influence on pattern 11 reveals some of the strongest anomalous frequencies, extending to surprisingly long lags (Fig. 10, right column). Positive anomalous frequencies occur about 35–40 days after MJO phase 1, although statistically significant anomalous frequencies at such long lags may be a random occurrence, as significant anomalous frequencies at these lags for all other MJO phases and SOM patterns are uncommon (not shown). These positive anomalous frequencies shift to smaller lags with increasing MJO phase, although not always remaining statistically significant. Nevertheless, this progression of anomalous frequencies is consistent with the eastward progression of the MJO convection with a time scale of ∼(40–50) days.

Overall the analysis of intraseasonal variability suggests that the 12 SOM patterns vary with a short intrinsic time scale on the order of one week, but there are potential sources of predictability that extend to lead times of several weeks. These sources may be related to extratropical atmospheric dynamics, as in the BAM, and excitation through tropical convection, as with the MJO.

c. Interannual variability

Figure 3 indicates that the 12 SOM patterns undergo substantial interannual variability in the pattern
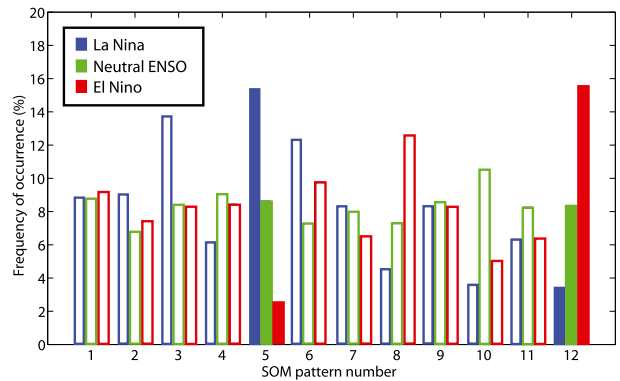

FIG. 11. Frequency of occurrence (%) of the 12 SOM patterns (x axis) during La Niña (blue), neutral ENSO (green), and El Niño (red) episodes. Filled bars indicate that the La Niña and El Niño frequencies are significantly different from the climatological frequency at the 5% level on the basis of a Monte Carlo resampling test described in the text.

frequency of occurrence. Moreover, the preceding section suggests that the tropics may play an important role in modulating these frequencies of occurrence. Here we examine whether the tropical convection anomalies associated with ENSO also may have a significant influence on SOM pattern frequency of occurrence. As discussed in section 2, we use a single index (Niño-3.4 SST) to partition the data into three standard ENSO categories, but it is likely that such a simple partitioning does not capture the full impact of ENSO variability, including different ENSO "flavors" (e.g., Johnson 2013), on the SOM patterns. Therefore, this analysis should be viewed as a first step to assess the influence of the three canonical ENSO categories. We also note that JJA is typically characterized by either the developing or decaying stage of ENSO, which indicates that ENSO-related SST anomalies are typically weaker than in austral summer.

Figure 11 presents the frequencies of occurrence of the 12 SOM patterns sorted by the three ENSO categories. Statistical significance of anomalous frequencies is assessed with a similar type of Monte Carlo resampling test as for the MJO-related anomalous frequencies. In this case we randomly reassign the dates of the El Niño and La Niña episodes in each simulation but maintain the average duration of each episode. We calculate the frequencies of occurrence for each SOM pattern and for each El Niño, neutral ENSO, and La Niña category in 10 000 simulations with the randomly reassigned ENSO categories. The ENSO-related frequencies are considered statistically significant at the 5% level if both of the observed SOM pattern frequencies during El Niño and La Niña exceed the 95%

confidence interval from the synthetic frequency calculations.

Figure 11 reveals that two patterns are significantly impacted by the occurrence of ENSO: patterns 5 and 12. Pattern 5, which projects onto the positive phase of the SAM but with strongest negative height anomalies centered over the Ross Sea covering the entire West Antarctica and extending to the George V coast (~150°E) (Figs. 2 and S6), is preferentially excited during La Niña and suppressed during El Niño. This general relationship between La Niña and the positive phase of the SAM is consistent with previous studies (L'Heureux and Thompson 2006; Fogt et al. 2011; Gong et al. 2013; Ding et al. 2012; Ding et al. 2015), although the tropical SST anomalies that force the SAM in JJA apparently are most significant in the central rather than eastern equatorial Pacific (Ding et al. 2012). Pattern 12, in contrast, is preferentially excited by El Niño. Interestingly, pattern 12 does not resemble the opposite phase of pattern 5, although it does feature positive height anomalies off the West Antarctic coast (Figs. 2 and S11). Pattern 12 can be characterized as a tripole pattern with positive height anomalies near the Amundsen Sea and the prime meridian and a negative height center over the Antarctic Peninsula. This SOM pattern resembles the composite Z500 anomaly pattern for El Niño episodes identified by Karoly (1989), which supports the consistency with previous work. The enhanced high-latitude Pacific ridging (troughing) during El Niño (La Niña) also is consistent with the enhanced (suppressed) occurrence of atmospheric blocking during El Niño (La Niña) (Oliveira et al. 2014). Note that the patterns most strongly excited by ENSO are distinct from the patterns most strongly connected with the MJO.

d. Interdecadal variability

As indicated by Fig. 3, some SOM patterns have undergone a substantial trend in frequency of occurrence over the 34-yr period under investigation. We provide the linear frequency of occurrence trend of all 12 SOM patterns in Fig. 12, which reveals that the patterns on the left side of the SOM have undergone negative frequency trends, whereas the patterns on the right have undergone a positive trend. Referring back to Figs. 2 and 4, we find that these results indicate positive frequency trends for negative SAM-like patterns, but negative frequency trends for positive SAM-like patterns. This trend toward the negative phase of the SAM in JJA, which starkly contrasts the trend in austral summer, has been noted previously (Ding et al. 2012). The figure further reveals that two particular patterns have experienced the strongest trends, a negative frequency trend for pattern 1 and a positive frequency trend for pattern 11.
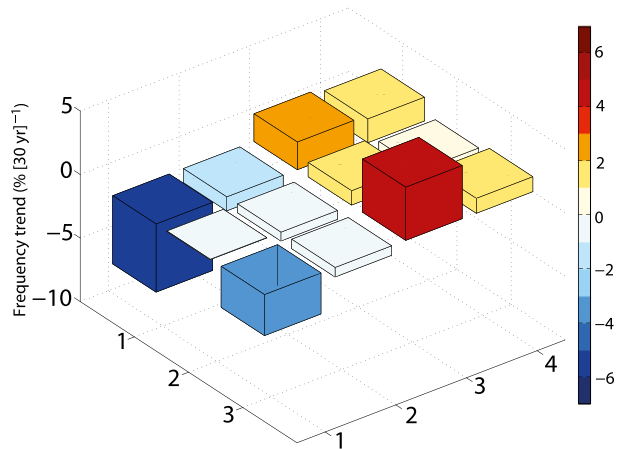

FIG. 12. SOM pattern frequency trends [% (30 yr)$^{-1}$] (z axis and color scale) over 1979–2012 for the 12 SOM patterns oriented in the same way as in Fig. 2 (x and y axes).

Because the trends in tropical SSTs have been implicated as important sources for extratropical SH trends (Ding et al. 2011, 2012; Ding and Steig 2013; Li et al. 2014; Ding et al. 2015), we examine the possible role of tropical convection in the positive frequency trend of SOM pattern 11. Figure 10 confirms a tropical connection with pattern 11, as the MJO is shown to strongly excite this pattern. We examine this connection more closely in Fig. 13, which presents lagged composites for pattern 11 calculated in the same way as in Figs. 6–8 but with tropical rainfall and upper tropospheric (sigma level 0.2582) streamfunction for lags between −12 days and +6 days. This figure reveals that the excitation of pattern 11 tends to be preceded by enhanced tropical convection in the equatorial western Pacific near and southeast of the Philippines about 6–12 days before the occurrence of pattern 11. Given that pattern 11 is strongly associated with the PSA2 (Fig. 4c), these results are consistent with Mo and Higgins (1998). Between lag −12 and −6 days, a wave train emanating from southern Africa intensifies while an east–west streamfunction dipole develops over and east of Australia that is reminiscent of the equatorial Rossby–Kelvin wave response typical of MJO episodes (e.g., Matthews et al. 2004). The wave train of wavenumber 4 intensifies further after lag −6 days and peaks at lag 0 (Fig. 13e).

Next we examine whether or not there has been a trend in the tropical precipitation patterns associated with the excitation of pattern 11. For this analysis we projected daily JJA precipitation fields from 30°S to 30°N onto the lag −6-, −9-, and −12-day precipitation composites of Fig. 13 and then determined whether or not a trend is evident. The trends of these projection time series are weak and far from statistical significance,
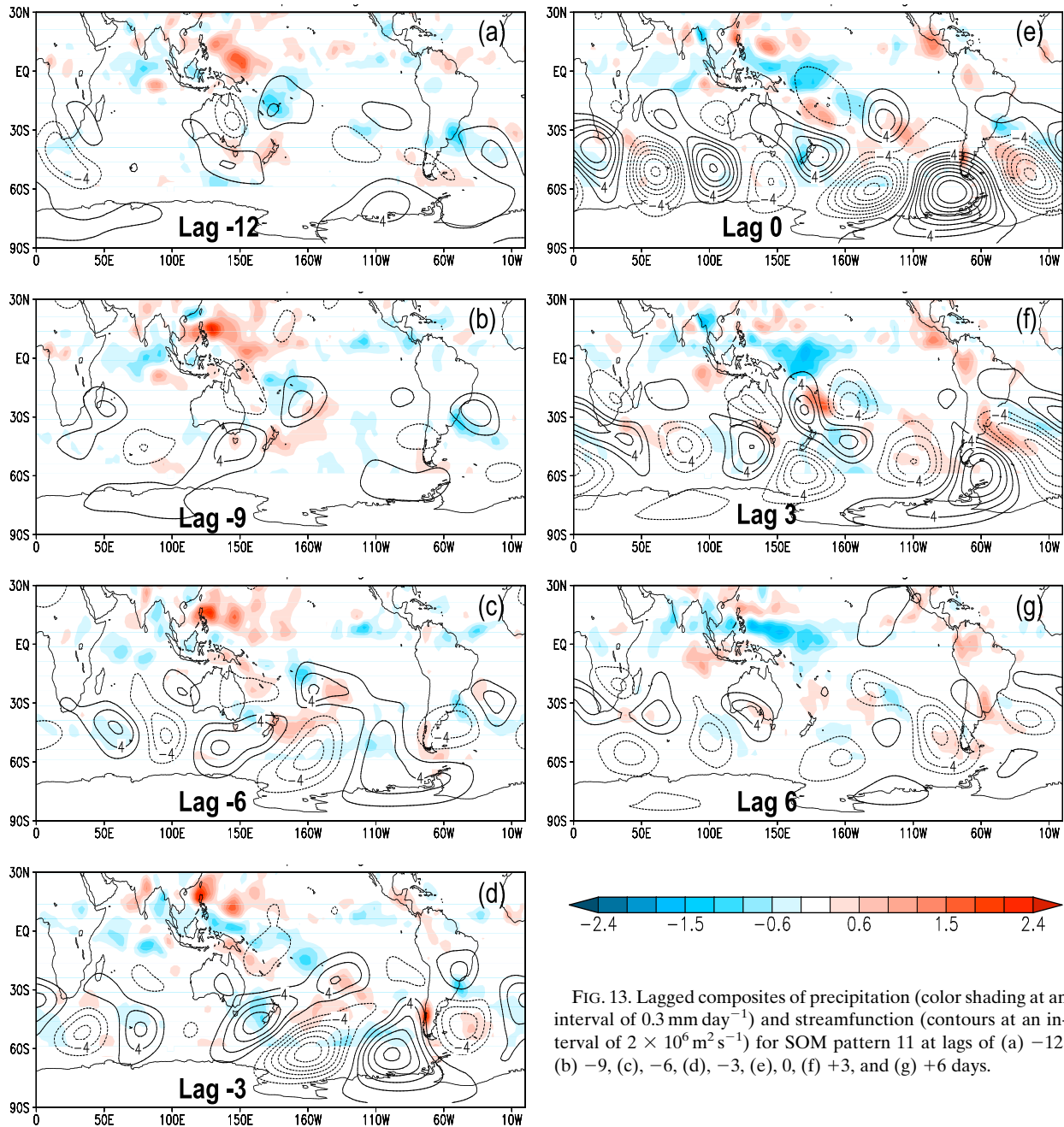
FIG. 13. Lagged composites of precipitation (color shading at an interval of 0.3 mm day^{-1}) and streamfunction (contours at an interval of 2×10^6 m^2 s^{-1}) for SOM pattern 11 at lags of (a) -12, (b) -9, (c) -6, (d) -3, (e) 0, (f) $+3$, and (g) $+6$ days.

indicating that there has not been a discernible increase in frequency of precipitation patterns known to excite SOM pattern 11. Figure 14 provides the 1979–2012 JJA trends of GPCP precipitation and 500-hPa geopotential height, further supporting that the trend in tropical precipitation does not match closely with the lagged composites of Fig. 13. Specifically, the centered pattern correlations between the tropical precipitation trend pattern from 30°S to 30°N (Fig. 14a) and the pattern 11 precipitation composites (Figs. 13a–c) are -0.06 for a

lag of -12 days, -0.04 for a lag of -9 days, and 0.00 for a lag of -6 days, which confirm the conclusion drawn from visual inspection.

Another possibility is that the trends in SOM pattern frequency relate to "climate noise" internal to the atmosphere—that is, arising from stochastic variability of atmospheric processes with short, intraseasonal time scales (Feldstein 2000a). Here we distinguish atmospheric internal variability from other forms of internal variability that incorporate coupling with the
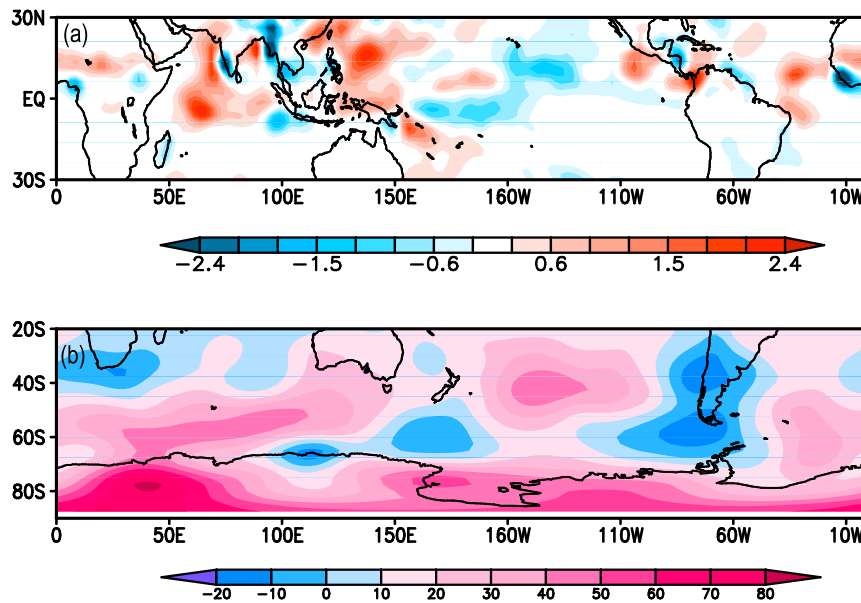
FIG. 14. Linear trends of JJA (a) GPCP tropical precipitation $[\text{mm day}^{-1} (30\,\text{yr})^{-1}]$ and (b) NCEP–NCAR extratropical SH 500-hPa geopotential height $[\text{m} (30\,\text{yr})^{-1}]$ for the 1979–2012 period.

hydrosphere and cryosphere, which would entail natural fluctuations of longer time scales. To explore the possible role of atmospheric internal variability, we examine the statistical significance of the 12 SOM frequency trends with respect to a K-state first-order Markov chain null hypothesis, similar to what was applied in Johnson (2013). For this test we generate 10 000 synthetic first-order Markov chain SOM pattern time series with the same transition probabilities as observed and then calculate the frequency trends from each of these synthetic time series. The observed SOM frequency trends are considered statistically significant at the 5% (10%) level if they are located outside the 95% (90%) confidence interval based on the distribution of 10 000 synthetic trends. Figure 15 reveals that all 12 SOM pattern frequency trends are not statistically significant at the 5% level, and only the trend for SOM pattern 1 is statistically significant at the 10% level. Because a first-order Markov chain is memoryless, these results suggest that the observed trends in wintertime SH teleconnections may have arisen from processes that are internal to the atmosphere, although a role for tropical SSTs cannot be ruled out.

4. Summary and conclusions

In this study we use the method of SOMs to characterize the continuum of wintertime teleconnections in the extratropical SH. We find that 12 SOM patterns describe a variety of teleconnections that project onto the SAM while also exhibiting PSA-like wave trains in the midtropospheric height field. Therefore, the continuum of teleconnection patterns present in the daily height fields generally exhibit properties that are a mix between the SAM and PSA.

All 12 patterns have intrinsic time scales of about 5–10 days, indicating that the patterns grow and decay on short, intraseasonal time scales. However, many patterns also exhibit significantly enhanced or suppressed frequencies of occurrence over longer intraseasonal time scales of ~(20–30) days in relation to the MJO and possibly the recently identified baroclinic annular mode (Thompson and Barnes 2014; Thompson and Woodworth 2014). In addition, two patterns respond strongly to the phase of ENSO on interannual time scales. Recently, Johnson et al. (2014) demonstrated that a simple statistical model based on the combined influence of the MJO and ENSO can yield skillful wintertime temperature forecasts over North America for lead times of up to four weeks. The results presented here suggest that similar potential may exist in the SH, and the BAM may offer another source of predictability not present in the Northern Hemisphere.

Longer-term trends in the SH climate respond to a variety of factors. In austral summer, ozone depletion has played a significant role in tropospheric circulation trends, likely contributing to a strong positive trend in the SAM (Arblaster and Meehl 2006; Polvani et al. 2011; Lee and Feldstein 2013). Tropical SST exerts significant influences on SH climate trends, mainly through
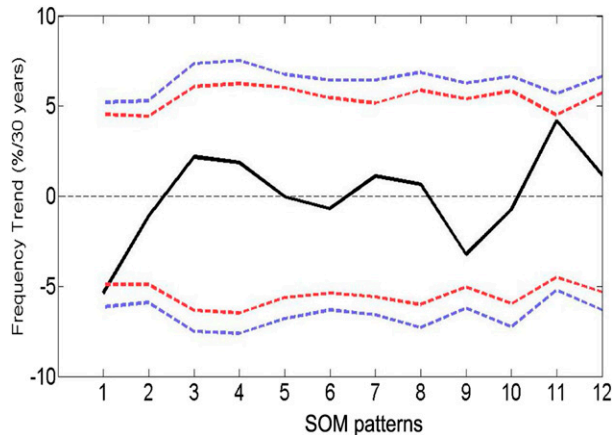
FIG. 15. SOM pattern frequency trends [% (30 yr)$^{-1}$] over 1979–2012 for the 12 SOM patterns (solid black) with the 90% (red dashed) and 95% (blue dashed) confidence intervals determined from the Markov chain simulations described in the text.

modifying patterns of tropical deep convection that force atmospheric teleconnection patterns (Ding et al. 2011; Schneider et al. 2012; Ding and Steig 2013; Li et al. 2014; Ding et al. 2015). In the Pacific, such a tropical linkage shows strong seasonality with the maximum amplitude of the South Pacific circulation anomaly in austral spring (Schneider et al. 2012) when the SH Rossby wave source is strongest (Jin and Kirtman 2009). Although previous studies suggest the importance of tropical low-frequency SST variability in forcing the SH climate trends in austral winter (Ding et al. 2011; Li et al. 2014), the tropical Pacific influence may be more robust in austral fall than in winter (Ding and Steig 2013). The results presented here support such a conclusion, as tropical forcing does not appear to play a dominant role in the frequency trends of the SOM patterns with the strongest trends. Moreover, the statistical tests we performed suggest that the observed atmospheric circulation trends in JJA are consistent with those that may arise from internal atmospheric variability alone. These results point out the potential importance of atmospheric "climate noise" in generating trends over the period from 1979 to 2012 in the dynamically active winter season, which then highlights the challenge of detecting external sources of atmospheric circulation trends over the course of a few decades (Deser et al. 2012).

The 12 SOM patterns that grow and decay over the course of less than 10 days also have a significant influence on the SIC fields on intraseasonal time scales, although the growth and decay of the SIC anomalies are of a somewhat longer time scale of ~(2–4) weeks. The resulting SIC anomaly patterns are consistent with the expected dynamic and thermodynamic influences of the atmospheric circulation, as they generally form in spatial

quadrature with the atmospheric circulation. This analysis, however, does not address the long-term positive trend of sea ice that has countered climate model projections (Turner et al. 2013), although the magnitude of this positive trend is uncertain due to inhomogeneities in the satellite-derived data (Eisenman et al. 2014). The interdecadal sea ice trend likely involves interactions and feedbacks among the atmospheric circulation, ice sheets, and ocean, but such analysis is reserved for future studies.

The continuum perspective and methodology presented here contrast the conventional teleconnection studies that identify a few unique patterns through EOF analysis. Although the EOF-based approach has advantages for quite a few problems, some potential advantages of the SOM-based approach are evident in this study. The 12-pattern SOM identifies a diverse set of teleconnection patterns that exhibit contrasting behavior. Some patterns are strongly excited by the MJO (i.e., patterns 1, 7, and 11), whereas others (i.e., patterns 2 and 6) exhibit evidence of quasi-oscillatory behavior unrelated to the MJO. Still others (i.e., patterns 5 and 12) are strongly excited by ENSO. SOM analysis provides a natural way of linking teleconnection patterns with short, intraseasonal time scales to climate variability on longer interannual and interdecadal time scales. The richness of this diversity is readily apparent by the approach taken here but likely would not emerge as clearly without a continuum perspective of SH teleconnection patterns.

REFERENCES

Adler, R. F., and Coauthors, 2003: The Version-2 Global Precipitation Climatology Project (GPCP) monthly precipitation

analysis (1979–present). *J. Hydrometeor.*, **4**, 1147–1167, doi:10.1175/1525-7541(2003)004<1147:TVGPCP>2.0.CO;2.

Arblaster, J. M., and G. A. Meehl, 2006: Contributions of external forcings to southern annular mode trends. *J. Climate*, **19**, 2896–2905, doi:10.1175/JCLI3774.1.

Benjamini, Y., and Y. Hochberg, 1995: Controlling the false discovery rate: A practical and powerful approach to multiple testing. *J. Roy. Stat. Soc.*, **57B**, 289–300.

Bromwich, D. H., J. P. Nicolas, A. J. Monaghan, M. A. Lazzara, L. M. Keller, G. A. Weidner, and A. B. Wilson, 2013: Central West Antarctica among the most rapidly warming regions on Earth. *Nat. Geosci.*, **6**, 139–145, doi:10.1038/ngeo1671.

Cassou, C., 2008: Intraseasonal interaction between the Madden–Julian oscillation and North Atlantic Oscillation. *Nature*, **455**, 523–527, doi:10.1038/nature07286.

Cavalieri, D. J., P. Gloersen, and W. J. Campbell, 1984: Determination of sea ice parameters with the Nimbus 7 SMMR. *J. Geophys. Res.*, **89**, 5355–5369, doi:10.1029/JD089iD04p05355.

——, C. L. Parkinson, N. DiGirolamo, and A. Ivanoff, 2012: Intersensor calibration between F13 SSMI and F17 SSMIS for global sea ice data records. *IEEE Geosci. Remote Sens. Lett.*, **9**, 233–236, doi:10.1109/LGRS.2011.2166754.

Dee, D. P., and Coauthors, 2011: The ERA-Interim reanalysis: Configuration and performance of the data assimilation system. *Quart. J. Roy. Meteor. Soc.*, **137**, 553–597, doi:10.1002/qj.828.

Deser, C., M. A. Alexander, S.-P. Xie, and A. S. Phillips, 2010: Sea surface temperature variability: Patterns and mechanisms. *Annu. Rev. Mar. Sci.*, **2**, 115–143, doi:10.1146/annurev-marine-120408-151453.

——, A. S. Phillips, V. Bourdette, and H. Teng, 2012: Uncertainty in climate change projections: The role of internal variability. *Climate Dyn.*, **38**, 527–546, doi:10.1007/s00382-010-0977-x.

Ding, H., R. J. Greatbatch, and G. Gollan, 2014: Tropical influence independent of ENSO on the austral summer southern annular mode. *Geophys. Res. Lett.*, **41**, 3643–3648, doi:10.1002/2014GL059987.

——, ——, and ——, 2015: Tropical impact on the interannual variability and long-term trend of the southern annular mode during austral summer from 1960/1961 to 2001/2002. *Climate Dyn.*, **44**, 2215–2228, doi:10.1007/s00382-014-2299-x.

Ding, Q., and E. J. Steig, 2013: Temperature change on the Antarctic Peninsula linked to the tropical Pacific. *J. Climate*, **26**, 7570–7585, doi:10.1175/JCLI-D-12-00729.1.

——, ——, D. S. Battisti, and M. Küttel, 2011: Winter warming in West Antarctica caused by central tropical Pacific warming. *Nat. Geosci.*, **4**, 398–403, doi:10.1038/ngeo1129.

——, ——, ——, and J. M. Wallace, 2012: Influence of the tropics on the southern annular mode. *J. Climate*, **25**, 6330–6348, doi:10.1175/JCLI-D-11-00523.1.

Eisenman, I., W. N. Meier, and J. R. Norris, 2014: A spurious jump in the satellite record: Has Antarctic sea ice expansion been overestimated? *Cryosphere*, **8**, 1289–1296, doi:10.5194/tc-8-1289-2014.

Feldstein, S. B., 2000a: Is interannual zonal mean flow variability simply climate noise? *J. Climate*, **13**, 2356–2362, doi:10.1175/1520-0442(2000)013<2356:IIZMFV>2.0.CO;2.

——, 2000b: Teleconnections and ENSO: The timescale, power spectra, and climate noise properties. *J. Climate*, **13**, 4430–4440, doi:10.1175/1520-0442(2000)013<4430:TTPSAC>2.0.CO;2.

Ferranti, L., T. N. Palmer, F. Molteni, and E. Klinker, 1990: Tropical–extratropical interaction associated with the 30–60 day oscillation and its impact on medium and extended range

prediction. *J. Atmos. Sci.*, **47**, 2177–2199, doi:10.1175/1520-0469(1990)047<2177:TEIAWT>2.0.CO;2.

Flatau, M., and Y.-J. Kim, 2013: Interaction between the MJO and polar circulations. *J. Climate*, **26**, 3562–3574, doi:10.1175/JCLI-D-11-00508.1.

Fogt, R. L., D. H. Bromwich, and K. M. Hines, 2011: Understanding the SAM influence on the South Pacific ENSO teleconnection. *Climate Dyn.*, **36**, 1555–1576, doi:10.1007/s00382-010-0905-0.

Franzke, C., and S. B. Feldstein, 2005: The continuum and dynamics of Northern Hemisphere teleconnection patterns. *J. Atmos. Sci.*, **62**, 3250–3267, doi:10.1175/JAS3536.1.

Gerber, E. P., L. M. Polvani, and D. Ancukiewicz, 2008: Annular mode time scales in the Intergovernmental Panel on Climate Change Fourth Assessment Report models. *Geophys. Res. Lett.*, **35**, L22707, doi:10.1029/2008GL035712.

Ghil, M., and K.-C. Mo, 1991: Intraseasonal oscillations in the global atmosphere. Part II: Southern Hemisphere. *J. Atmos. Sci.*, **48**, 780–790, doi:10.1175/1520-0469(1991)048<0780:IOITGA>2.0.CO;2.

Gong, T., S. B. Feldstein, and D. Luo, 2013: A simple GCM study on the relationship between ENSO and the southern annular mode. *J. Atmos. Sci.*, **70**, 1821–1832, doi:10.1175/JAS-D-12-0161.1.

Hande, L. B., S. T. Siems, and M. J. Manton, 2012: Observed trends in wind speed over the Southern Ocean. *Geophys. Res. Lett.*, **39**, L11802, doi:10.1029/2012GL051734.

Hartmann, D. L., and F. Lo, 1998: Wave-driven zonal flow vacillation in the Southern Hemisphere. *J. Atmos. Sci.*, **55**, 1303–1315, doi:10.1175/1520-0469(1998)055<1303:WDZFVI>2.0.CO;2.

Hewitson, B. C., and R. G. Crane, 2002: Self-organizing maps: Applications to synoptic climatology. *Climate Res.*, **22**, 13–26, doi:10.3354/cr022013.

Holland, P. R., and R. Kwok, 2012: Wind-driven trends in Antarctic sea-ice drift. *Nat. Geosci.*, **5**, 872–875, doi:10.1038/ngeo1627.

Hoskins, B. J., and D. J. Karoly, 1981: The steady linear response of a spherical atmosphere to thermal and orographic forcing. *J. Atmos. Sci.*, **38**, 1179–1196, doi:10.1175/1520-0469(1981)038<1179:TSLROA>2.0.CO;2.

Hurrell, J. W., and H. van Loon, 1994: A modulation of the atmospheric annual cycle in the Southern Hemisphere. *Tellus*, **46A**, 325–338, doi:10.1034/j.1600-0870.1994.t01-1-00007.x.

Jin, D., and B. P. Kirtman, 2009: Why the Southern Hemisphere ENSO responses lead ENSO. *J. Geophys. Res.*, **114**, D23101, doi:10.1029/2009JD012657.

Johnson, N. C., 2013: How many ENSO flavors can we distinguish? *J. Climate*, **26**, 4816–4827, doi:10.1175/JCLI-D-12-00649.1.

——, and S. B. Feldstein, 2010: The continuum of North Pacific sea level pressure patterns: Intraseasonal, interannual, and interdecadal variability. *J. Climate*, **23**, 851–867, doi:10.1175/2009JCLI3099.1.

——, ——, and B. Tremblay, 2008: The continuum of Northern Hemisphere teleconnection patterns and a description of the NAO shift with the use of self-organizing maps. *J. Climate*, **21**, 6354–6371, doi:10.1175/2008JCLI2380.1.

——, D. C. Collins, S. B. Feldstein, M. L. L'Heureux, and E. E. Riddle, 2014: Skillful wintertime North American temperature forecasts out to 4 weeks based on the state of ENSO and the MJO. *Wea. Forecasting*, **29**, 23–38, doi:10.1175/WAF-D-13-00102.1.

Kalnay, E., and Coauthors, 1996: The NCEP/NCAR 40-Year Reanalysis Project. *Bull. Amer. Meteor. Soc.*, **77**, 437–471, doi:10.1175/1520-0477(1996)077<0437:TNYRP>2.0.CO;2.

Karoly, D. J., 1989: Southern Hemisphere circulation features associated with El Niño–Southern Oscillation events. *J. Climate*, **2**, 1239–1252, doi:10.1175/1520-0442(1989)002<1239:SHCFAW>2.0.CO;2.

Kohonen, T., 2001: *Self-Organizing Maps.* Springer, 501 pp.

Lau, K.-M., P.-J. Sheu, and I.-S. Kang, 1994: Multiscale low-frequency circulation modes in the global atmosphere. *J. Atmos. Sci.*, **51**, 1169–1193, doi:10.1175/1520-0469(1994)051<1169:MLFCMI>2.0.CO;2.

Lee, S., and S. B. Feldstein, 2013: Detecting ozone- and greenhouse gas–driven wind trends with observational data. *Science*, **339**, 563–567, doi:10.1126/science.1225154.

——, T. Gong, N. Johnson, S. Feldstein, and D. Pollard, 2011: On the possible link between tropical convection and the Northern Hemisphere Arctic surface air temperature change between 1958 and 2001. *J. Climate*, **24**, 4350–4367, doi:10.1175/2011JCLI4003.1.

L'Heureux, M. L., and D. W. J. Thompson, 2006: Observed relationships between the El Niño–Southern Oscillation and the extratropical zonal-mean circulation. *J. Climate*, **19**, 276–287, doi:10.1175/JCLI3617.1.

——, and R. W. Higgins, 2008: Boreal winter links between the Madden–Julian oscillation and the Arctic Oscillation. *J. Climate*, **21**, 3040–3050, doi:10.1175/2007JCLI1955.1.

Li, X., D. M. Holland, E. P. Gerber, and C. Yoo, 2014: Impacts of the north and tropical Atlantic Ocean on the Antarctic Peninsula and sea ice. *Nature*, **505**, 538–542, doi:10.1038/nature12945.

Lin, H., G. Brunet, and J. Derome, 2009: An observed connection between the North Atlantic Oscillation and the Madden–Julian oscillation. *J. Climate*, **22**, 364–380, doi:10.1175/2008JCLI2515.1.

Liu, Y., R. H. Weisberg, and C. N. K. Mooers, 2006: Performance evaluation of the self-organizing map for feature extraction. *J. Geophys. Res.*, **111**, C05018, doi:10.1029/2005JC003117.

Madden, R. A., and P. R. Julian, 1971: Detection of a 40–50 day oscillation in the zonal wind in the tropical Pacific. *J. Atmos. Sci.*, **28**, 702–708, doi:10.1175/1520-0469(1971)028<0702:DOADOI>2.0.CO;2.

——, and ——, 1972: Description of global-scale circulation cells in the tropics with a 40–50 day period. *J. Atmos. Sci.*, **29**, 1109–1123, doi:10.1175/1520-0469(1972)029<1109:DOGSCC>2.0.CO;2.

Marshall, G. J., 2003: Trends in the southern annular mode from observations and reanalyses. *J. Climate*, **16**, 4134–4143, doi:10.1175/1520-0442(2003)016<4134:TITSAM>2.0.CO;2.

Matthews, A. J., and M. P. Meredith, 2004: Variability of Antarctic circumpolar transport and the southern annular mode associated with the Madden–Julian oscillation. *Geophys. Res. Lett.*, **31**, L24312, doi:10.1029/2004GL021666.

——, B. J. Hoskins, and M. Masutani, 2004: The global response to tropical heating in the Madden–Julian oscillation during the northern winter. *Quart. J. Roy. Meteor. Soc.*, **130**, 1991–2011, doi:10.1256/qj.02.123.

Meehl, G. A., J. W. Hurrell, and H. van Loon, 1998: A modulation of the mechanism of the semiannual oscillation in the Southern Hemisphere. *Tellus*, **50A**, 442–450, doi:10.1034/j.1600-0870.1998.t01-3-00005.x.

Mo, K. C., 2000: Relationships between interdecadal variability in the Southern Hemisphere and sea surface temperature anomalies. *J. Climate*, **13**, 3599–3610, doi:10.1175/1520-0442(2000)013<3599:RBLFVI>2.0.CO;2.

——, and M. Ghil, 1987: Statistics and dynamics of persistent anomalies. *J. Atmos. Sci.*, **44**, 877–902.

——, and R. W. Higgins, 1998: The Pacific–South American modes and tropical convection during the Southern Hemisphere winter. *Mon. Wea. Rev.*, **126**, 1581–1596, doi:10.1175/1520-0493(1998)126<1581:TPSAMA>2.0.CO;2.

——, and J. N. Paegle, 2001: The Pacific–South American modes and their downstream effects. *Int. J. Climatol.*, **21**, 1211–1229, doi:10.1002/joc.685.

Mori, M., and M. Watanabe, 2008: The growth and triggering mechanisms of the PNA: A MJO-PNA coherence. *J. Meteor. Soc. Japan*, **86**, 213–236, doi:10.2151/jmsj.86.213.

North, G. R., T. L. Bell, R. F. Cahalan, and F. J. Moeng, 1982: Sampling errors in the estimation of empirical orthogonal functions. *Mon. Wea. Rev.*, **110**, 699–706, doi:10.1175/1520-0493(1982)110<0699:SEITEO>2.0.CO;2.

Oliveira, F. N. M., L. M. V. Carvalho, and T. Ambrizzi, 2014: A new climatology for Southern Hemisphere blockings in the winter and the combined effect of ENSO and SAM phases. *Int. J. Climatol.*, **34**, 1676–1692, doi:10.1002/joc.3795.

Polvani, L. M., D. W. Waugh, G. J. P. Correa, and S.-W. Son, 2011: Stratospheric ozone depletion: The main driver of twentieth-century atmospheric circulation changes in the Southern Hemisphere. *J. Climate*, **24**, 795–812, doi:10.1175/2010JCLI3772.1.

Reusch, D. B., R. B. Alley, and B. C. Hewitson, 2005: Relative performance of self-organizing maps and principal component analysis in pattern extraction from synthetic climatological data. *Polar Geogr.*, **29**, 188–212, doi:10.1080/789610199.

——, ——, and ——, 2007: North Atlantic climate variability from a self-organizing map perspective. *J. Geophys. Res.*, **112**, D02104, doi:10.1029/2006JD007460.

Revell, M. J., J. W. Kidson, and G. N. Kiladis, 2001: Interpreting low-frequency modes of Southern Hemisphere atmospheric variability as the rotational response to divergent forcing. *Mon. Wea. Rev.*, **129**, 2416–2425, doi:10.1175/1520-0493(2001)129<2416:ILFMOS>2.0.CO;2.

Riddle, E. E., M. B. Stoner, N. C. Johnson, M. L. L'Heureux, D. C. Collins, and S. B. Feldstein, 2013: The impact of the MJO on clusters of wintertime circulation anomalies over the North American region. *Climate Dyn.*, **40**, 1749–1766, doi:10.1007/s00382-012-1493-y.

Robertson, A. W., and C. R. Mechoso, 2003: Circulation regimes and low-frequency oscillations in the South Pacific sector. *Mon. Wea. Rev.*, **131**, 1566–1576, doi:10.1175/2548.1.

Santer, B. D., T. M. L. Wigley, and P. D. Jones, 1993: Correlation methods in fingerprint detection studies. *Climate Dyn.*, **8**, 265–276, doi:10.1007/BF00209666.

Schneider, D. P., Y. Okumura, and C. Deser, 2012: Observed Antarctic interannual climate variability and tropical linkages. *J. Climate*, **25**, 4048–4066, doi:10.1175/JCLI-D-11-00273.1.

Screen, J. A., 2011: Sudden increase in Antarctic sea ice: Fact or artifact? *Geophys. Res. Lett.*, **38**, L13702, doi:10.1029/2011GL047553.

——, and I. Simmonds, 2012: Half-century air temperature change above Antarctica: Observed trends and spatial reconstructions. *J. Geophys. Res.*, **117**, D16108, doi:10.1029/2012JD017885.

Singh, D., and Coauthors, 2014: Severe precipitation in northern India in June 2013: Causes, historical context, and changes in probability [in "Explaining Extremes of 2013 from a Climate Perspective"]. *Bull. Amer. Meteor. Soc.*, **95**, S58–S61.

Smith, T. M., R. W. Reynolds, T. C. Peterson, and J. Lawrimore, 2008: Improvements to NOAA's historical merged land–ocean surface temperature analysis (1880–2006). *J. Climate*, **21**, 2283–2296, doi:10.1175/2007JCLI2100.1.

Stammerjohn, S. E., D. G. Martinson, R. C. Smith, X. Yuan, and D. Rind, 2008: Trends in Antarctic annual sea ice retreat and advance and their relation to El Niño–Southern Oscillation and southern annular mode variability. *J. Geophys. Res.*, **113**, C03S90, doi:10.1029/2007JC004269.

Steig, E. J., D. P. Schneider, S. D. Rutherford, M. E. Mann, J. C. Comiso, and D. T. Shindell, 2009: Warming of the Antarctic ice sheet surface since the 1957 International Geophysical Year. *Nature*, **457**, 459–462, doi:10.1038/nature07669.

Thompson, D. W. J., and J. M. Wallace, 2000: Annular modes in the extratropical circulation. Part I: Month-to-month variability. *J. Climate*, **13**, 1000–1016, doi:10.1175/1520-0442(2000)013<1000:AMITEC>2.0.CO;2.

——, and S. Solomon, 2002: Interpretation of recent Southern Hemisphere climate change. *Science*, **296**, 895–899, doi:10.1126/science.1069270.

——, and E. A. Barnes, 2014: Periodic variability in the large-scale Southern Hemisphere atmospheric circulation. *Science*, **343**, 641–645, doi:10.1126/science.1247660.

——, and J. D. Woodworth, 2014: Barotropic and baroclinic annular variability in the Southern Hemisphere. *J. Atmos. Sci.*, **71**, 1480–1493, doi:10.1175/JAS-D-13-0185.1.

Turner, J., T. J. Bracegirdle, T. Phillips, G. J. Marshall, and J. S. Hosking, 2013: An initial assessment of Antarctic sea ice extent in the CMIP5 models. *J. Climate*, **26**, 1473–1484, doi:10.1175/JCLI-D-12-00068.1.

Wheeler, M. C., and H. H. Hendon, 2004: An all-season real-time multivariate MJO index: Development of an index for monitoring and prediction. *Mon. Wea. Rev.*, **132**, 1917–1932, doi:10.1175/1520-0493(2004)132<1917:AARMMI>2.0.CO;2.

Wilks, D. S., 2006: On "field significance" and the false discovery rate. *J. Appl. Meteor. Climatol.*, **45**, 1181–1189, doi:10.1175/JAM2404.1.

Xue, Y., T. M. Smith, and R. W. Reynolds, 2003: Interdecadal changes of 30-yr SST normals during 1871–2000. *J. Climate*, **16**, 1601–1612, doi:10.1175/1520-0442-16.10.1601.

Yoo, C., S. Lee, and S. B. Feldstein, 2012a: The impact of the Madden–Julian oscillation trend on the Antarctic warming during the 1979–2008 austral winter. *Atmos. Sci. Lett.*, **13**, 194–199, doi:10.1002/asl.379.

——, ——, and ——, 2012b: Mechanisms of Arctic surface air temperature change in response to the Madden–Julian oscillation. *J. Climate*, **25**, 5777–5790, doi:10.1175/JCLI-D-11-00566.1.

Young, I. R., S. Zieger, and A. V. Babanin, 2011: Global trends in wind speed and wave height. *Science*, **332**, 451–455, doi:10.1126/science.1197219.

Zhang, C., 2005: Madden–Julian oscillation. *Rev. Geophys.*, **43**, RG2003, doi:10.1029/2004RG000158.

——, 2013: Madden–Julian oscillation: Bridging weather and climate. *Bull. Amer. Meteor. Soc.*, **94**, 1849–1870, doi:10.1175/BAMS-D-12-00026.1.